



저작자표시-비영리-변경금지 2.0 대한민국

이용자는 아래의 조건을 따르는 경우에 한하여 자유롭게

- 이 저작물을 복제, 배포, 전송, 전시, 공연 및 방송할 수 있습니다.

다음과 같은 조건을 따라야 합니다:



저작자표시. 귀하는 원저작자를 표시하여야 합니다.



비영리. 귀하는 이 저작물을 영리 목적으로 이용할 수 없습니다.



변경금지. 귀하는 이 저작물을 개작, 변형 또는 가공할 수 없습니다.

- 귀하는, 이 저작물의 재이용이나 배포의 경우, 이 저작물에 적용된 이용허락조건을 명확하게 나타내어야 합니다.
- 저작권자로부터 별도의 허가를 받으면 이러한 조건들은 적용되지 않습니다.

저작권법에 따른 이용자의 권리는 위의 내용에 의하여 영향을 받지 않습니다.

이것은 [이용허락규약\(Legal Code\)](#)을 이해하기 쉽게 요약한 것입니다.

[Disclaimer](#)

이학박사학위논문

**Hybrid photonic crystal lasers composed  
of passive structural backbone and active  
colloidal quantum dots**

능동형의 콜로이드 양자점과 수동형의 뼈대  
구조로 이루어진 하이브리드 광자결정 레이저

2018년 8월

서울대학교 대학원

물리천문학부

정 현 호



**Hybrid photonic crystal lasers composed  
of passive structural backbone and active  
colloidal quantum dots**

by  
Hyunho Jung

Supervised by  
Professor Heonsu Jeon

*A Dissertation Submitted to the Faculty of  
Seoul National University  
in Partial Fulfillment of the Requirements  
for the Degree of  
Doctor of Philosophy*

August 2018

Department of Physics and Astronomy  
Graduate School  
Seoul National University







# Abstract

## **Hybrid photonic crystal lasers composed of passive structural backbone and active colloidal quantum dots**

Hyunho Jung

Department of Physics and Astronomy

The Graduate School

Seoul National University

A photonic crystal (PhC) is a periodic structure in which two or more materials having different dielectric constants are arranged on a wavelength scale of an electromagnetic wave. The structure affects the motion of photons in the similar manner that ionic lattices affects the motion of electrons in the periodic potential. The electromagnetic waves passing through the PhC have an extraordinary photonic dispersion relation that cannot be found when the waves passing through a homogeneous medium. Photonic band-gap and group-velocity anomalies in dispersion are representative optical properties in PhC. The photonic band-gap is a frequency region where the states of the photon cannot exist. Also, photonic band-edge as an anomaly is a region in which the group velocity of photonic modes approaches zero. Two notions about photonic states can be used for confining the electromagnetic waves in strongly localized cavity structures or spatially extended standing-wave resonance forms and interaction between optical gain materials and

photons can be remarkably increased.

PhC have great potential in that they can be fabricated in small areas and have low power consumption in generating coherent light source. Also, the PhC can be utilized for an efficient light source having designed modal properties for photonic integrated circuits (PICs). Hybrid PhC lasers, coherent light sources composed of a passive optical structure and external active gain materials, have a flexibility in selecting source wavelengths and waveguiding properties so that can be prominent coherent sources to realizing high density PICs. Especially, colloidal quantum dots (CQDs) are one of promising gain materials in future PICs picture. CQDs are efficiently light-emitting building blocks of nano-sizes synthesized by low-cost, solution-processed chemistry. Also, spectrally narrow emission wavelengths of CQDs are easily tunable by controlling the size of individual CQDs without deteriorating quantum efficiency.

In this thesis, in the first research topic, efficient platform for on-chip integration of CQD PhC laser and passive components is suggested. Silicon nitride is interesting material, which can be treated by CMOS-compatible process and also has relatively high refractive index and broad optical transparency from visible to near-infrared wavelength range. With combination of silicon nitride and CQDs gain materials, hybrid PhC lasers and passive devices are efficiently integrated in a way where silicon nitride waveguiding layer is shared by various components. A conceptual PIC is experimentally demonstrated, in which a PhC band-edge laser, a slab waveguide, and output couplers are all integrated on a single chip. Under excitation condition, coherent single-mode laser is emitted with well-defined in-plane emission directions, and subsequently coupled into the passive waveguide layer with a guaranteed high coupling efficiency. This configuration for active and passive photonic devices on a

chip could be an alternative picture of conventional silicon-based PIC in near future.

In the second research topic, continuously tunable distributed feedback (DFB) laser device composed of CQD film on chirped grating is introduced. To make hybrid type tunable laser source composed of CQDs and fused silica, high-throughput laser interference lithography (LIL) method is employed instead of writing the entire nano-patterns by conventional electron beam lithography. To make efficiently line gratings chirped, Lloyd's LIL configuration is modified by introducing cylindrical mirror parts. Also, CQD film is transferred onto wet-transfer method, which are intended for flat and dense CQD film to be positioned on the arbitrary substrate. Single-mode, surface-emitting DFB laser structures are numerically designed by finite-domain time-domain (FDTD) method. Also, laser wavelengths are observed to be progressively varied as optical excitation positions are translated in photoluminescence experiments. Continuously tunable coherent light source could be useful itself in a variety of applications. Moreover, the results demonstrate modified LIL method can produce high quality chirped gratings at less effort, which could be helpful for other sophisticated photonic devices.

In the appendant topic, bio-compatible silk DFB laser with physically transient characteristics are demonstrated. It is a kind of bio-compatible version of hybrid PhC laser composed of silk, fused silica, dyes. Silk fibroin is natural protein extracted from *Bombyx mori* caterpillar and draw public attention for its self-assembling property at optical wavelengths scale and optical transparency. The silk bio-ink, bio-compatible silk materials combined with sodium fluorescein dye commonly used for diagnostics in ophthalmology and optometry, is spin-casted on the robust fused silica grating substrate for DFB lasing. The organic device has limited lifetime due to the degradability of dye but silk active layer can be easily removed by dipping in water,

and by re-coating the bio-ink new device can be obtained without difficulties. In addition, chemo-sensing capability for detecting hydrochloride vapor is also investigated.

In conclusion, in this these, I suggest hybrid type PhC laser of passive structural backbone and external gain material, especially CQDs. Efficient on-chip integrated coherent laser sources with passive structures are demonstrated, and tunable laser sources from efficient fabrication method are presented. These results are expected to contribute to the understanding of various optical devices and PIC, as well as to the efficient implementation.

**Keyword:** Photonic crystal, Hybrid photonic crystal lasers, Colloidal quantum dots,  
On-chip integration, Tunable laser

**Student number:** 2011-20424

# Contents

## Chapter 1

<b>Introduction</b> .....	<b>1</b>
1.1. Coherent light source .....	1
1.1.1. Semiconductor lasers .....	2
1.1.2. Laser source for high-density photonic integration .....	4
1.2. Photonic crystals .....	6
1.2.1. Introduction.....	6
1.2.2. Photonic band structure.....	7
1.2.3. Photonic crystal band-edge laser.....	9
1.2.4. Photonic crystal cavity laser .....	11
1.3. Hybrid photonic crystal laser .....	13
1.4. Computational method.....	18
1.4.1. Plane wave expansion method .....	18
1.4.2. Finite-difference time-domain method .....	19
1.5. Outline of the manuscript.....	20
References.....	21

## Chapter 2

<b>Efficient platform for on-chip integration of colloidal quantum dot photonic crystal band-edge laser based on silicon nitride waveguide.....</b>	<b>27</b>
2.1. Introduction.....	27
2.2. Device design and calculation.....	29
2.2.1. Photonic integration of active and passive devices.....	29
2.2.2. Photonic band structure of colloidal quantum dots photonic crystal laser....	33
2.3. Device fabrication.....	37
2.4. Optical measurements and analyses.....	39
2.4.1. Optical measurements set-up .....	39
2.4.2. Laser emission properties of two symmetric points.....	40
2.4.3. Polarization dependence of laser emission .....	45
2.5. Summary .....	48
References.....	49

## Chapter 3

<b>Continuously tunable colloidal quantum dot distributed feedback lasers integrated on chirped grating .....</b>	<b>51</b>
3.1. Introduction.....	51
3.2. Device design and calculation.....	53
3.2.1. Continuously tunable distributed feedback laser .....	53
3.3. Device fabrication.....	57
3.3.1. Chirped grating generated by laser interference technique.....	57
3.3.2. Wet transfer of colloidal quantum dots film.....	60
3.3.3. Continuously tunable laser device .....	61
3.4. Optical measurements and analyses.....	62
3.4.1. Distributed feedback laser characteristics.....	62
3.4.2. Position dependence of the laser.....	65
3.5. Summary .....	67
References.....	68

## **Appendix**

<b>Distributed feedback laser with physically transient characteristics using bio-compatible fluorescein-doped silk solution.....</b>	<b>73</b>
A.1. Introduction.....	73
A.2. Device design and fabrication.....	76
A.2.1. Physically transient distributed feedback laser using silk-bio ink .....	76
A.2.2. Preparing silk bio-ink.....	77
A.2.3. Fluorescein doped-silk distributed feedback laser .....	78
A.3. Optical measurements and analyses.....	81
A.3.1. Optical characteristics of the physically transient distributed feedback laser .....	81
A.3.2. Application as a chemosensor to detect hydrogen chloride vapor .....	85
A.4. Summary .....	88
References.....	89

## **Chapter 4**

<b>Conclusion and perspective.....</b>	<b>95</b>
Abstract in Korean .....	98

# List of Figures

Figure 1-1-1 Absorption of a photon and generation of a stimulated photon .....	2
Figure 1-1-2 Conceptual image of PICs .....	5
Figure 1-2-1 Examples of 1D, 2D, and 3D PhCs.....	6
Figure 1-2-2 Photonic band structure of a 2D hexagonal lattice PhC.....	8
Figure 1-2-3 2D hexagonal lattice PhC band-edge laser .....	10
Figure 1-2-4 Schematic drawing of single-defect PhC cavity laser.....	11
Figure 1-2-5 Single-defect PhC cavity laser .....	12
Figure 1-3-1 Hybrid PhC band-edge laser. ....	13
Figure 1-3-2 Hybrid PhC cavity laser .....	14
Figure 1-3-3 CQDs with different diameters exhibiting various colors.....	15
Figure 1-3-4 Schematic diagram of energy levels in CQDs. ....	16
Figure 1-3-5 Structure of CdSe/CdS/ZnS CQDs .....	16
Figure 1-3-6 Photoluminescence emission spectrum of red CQDs .....	17
Figure 1-3-7 Complex refractive index of red CQDs. ....	17
Figure 2-1-1 Complex refractive index of a silicon nitride film.....	28
Figure 2-2-1 Schematic of on-chip integration of PhC band-edge laser, waveguide, and output coupler .....	30
Figure 2-2-2 Refractive index profiles (left) and fundamental TE-guided mode profiles (right) of the CQD–PhC band-edge laser section (red) and Si <sub>3</sub> N <sub>4</sub> waveguide section (blue) at a wavelength of 615 nm.....	31

Figure 2-2-3 FDTD-simulated TE-guided mode propagation across the interface between the CQD–PhC laser structure and the Si <sub>3</sub> N <sub>4</sub> waveguide.....	31
Figure 2-2-4 FDTD simulation near the joint between the waveguide and the grating coupler .....	32
Figure 2-2-5 Photonic band structure of the 2D square-lattice PhC calculated by the plane-wave expansion method.....	35
Figure 2-2-6 Resonant mode spectra & mode profiles calculated for the (a) X and (b) M symmetry points .....	36
Figure 2-2-7 FDTD-simulated propagation of band-edge mode. Profile of electric field magnitude at (a) X-point (X <sub>3</sub> /X <sub>4</sub> ) and at (b) M-point (M <sub>3</sub> /M <sub>4</sub> ).....	36
Figure 2-3-1 Optical microscope image and SEM images of integrated devices ....	38
Figure 2-4-1 Schematically illustrated micro-PL setup .....	39
Figure 2-4-2 Emission properties of the CQD–PhC X-point band-edge laser. (a) Photoluminescence spectra at various excitation pulse energies. (b) Light input versus light output relationship.....	41
Figure 2-4-3 Emission properties of the CQD–PhC M-point band-edge laser. (a) Photoluminescence spectra at various excitation pulse energies. (b) Light input versus light output relationship.....	42
Figure 2-4-4 Emission properties of the CQD–PhC X-point band-edge laser. (a) CCD image of below laser threshold. (b) CCD image of above laser threshold (c) Emission spectrum of the device under optical excitation below laser threshold. (d) Emission spectrum of the device under optical excitation above laser threshold .....	43

Figure 2-4-5 Emission properties of the CQD–PhC M-point band-edge laser. (a) CCD image of below laser threshold. (b) CCD image of above laser threshold (c) Emission spectrum of the device under optical excitation below laser threshold. (d) Emission spectrum of the device under optical excitation above laser threshold .....	44
Figure 2-4-6 Polarized emission properties of the X-point sample above threshold (a) CCD image at 0° polarization angle (b) CCD image at 90° polarization angle (c) Emission spectrum of the device at 0° polarization angle (d) Emission spectrum of the device at 90° polarization angle.....	46
Figure 2-4-7 Polarized emission properties of the M-point sample above threshold (a) CCD image at 45° polarization angle (b) CCD image at 135° polarization angle (c) Emission spectrum of the device at 45° polarization angle (d) Emission spectrum of the device at 135° polarization angle .....	47
Figure 3-2-1 Schematic of continuously tunable CQD-DFB laser .....	53
Figure 3-2-2 CQD film thickness dependence of effective index of fundamental guided modes. Yellow dashed line indicates film thickness of fabricated device.....	55
Figure 3-2-3 Dispersion relation of DFB laser near photonic band-edge .....	55
Figure 3-2-4 FDTD-simulated electric field profile of TE resonance mode.....	56
Figure 3-2-5 Tunability of DFB laser wavelength. Mode wavelengths are calculated by FDTD method .....	56
Figure 3-3-1 Modified Lloyd’s mirror stage by using cylindrical mirror .....	58
Figure 3-3-2 Detailed picture of cylindrical mirror stage .....	59

Figure 3-3-3 Calculation of tunability of period of chirped grating. For an incident angle ( $\theta_1 = 30.41^\circ$ ), grating period ranges are plotted .....	59
Figure 3-3-4 (a) SEM image of wet-transferred CQD film. (b) AFM image of a wet-transferred CQD film .....	60
Figure 3-3-5 (a) Photograph images of the sample. (b) SEM image of fabricated DFB laser. Upper right image shows magnified layered structure .....	61
Figure 3-4-1 Photoluminescence spectra at various excitation pulse energies .....	63
Figure 3-4-2 Light-in vs. light-out. (magenta), linewidth depending on pump energy (dark blue).....	63
Figure 3-4-3 Polarization distribution. Grating lines are parallel to $0^\circ$ , $180^\circ$ directions .....	64
Figure 3-4-4 Position dependence of lasing wavelength. Experimental data are shown as magenta color and calculation data are plotted as dark blue for comparison. 66	66
Figure 3-4-5 (a) Selected laser spectra taken at equal interval of $600 \mu\text{m}$ . (b) Threshold density variation over sample position .....	66
Figure A-2-1 Schematic configurations to show the working principle of the physically transient DFB laser using optically activated silk bio-ink and a permanently usable fused silica grating.....	76
Figure A-2-2 (a) Scanning electron microscopy (SEM) image of the fused silica grating generated by the laser-interference-lithography (LIL) method. (b) Absorption (dashed curve) and photoluminescence (solid curve) spectra for a thin film of sodium fluorescein doped silk. (c) Cross-sectional SEM image of the silk bio-ink coated fused silica grating. (d) Atomic force microscopy (AFM)	

topographic image of the sample in (c).....	79
Figure A-2-3 (a) Simulated spectrum of the DFB structure. (b) Normalized electric field (parallel to the grating surface) intensity corresponding to the resonance mode at $\lambda = 554.9$ nm .....	80
Figure A-2-4 Optical characteristics of the physically transient DFB laser. (a) Output energies of the lasing peak as a function of the pump influence. (b) Lasing spectra from the DFB laser. The lasing peak disappeared after washing out and reappeared after spin-coating the silk bio-ink .....	82
Figure A-2-5 Dependence of the DFB laser on sodium fluorescein concentration. Light-in versus light-out curves for three different concentrations .....	83
Figure A-2-6 Measured output energy as a function of the operating time .....	84
Figure A-2-7 Application as a chemosensor to detect HCl vapor. (a) Lasing spectra showing the responses before and after exposure to HCl vapor. Inset shows a photograph image of the silk DFB laser. (b) Absorption and PL spectra before and after 1 minute exposure to HCl vapor.....	86
Figure A-2-8 Transmission of the pure silk film on quartz substrate before/after exposure to HCl vapor. Insets show photographs of the clearance and transparency of the silk film.....	87



# Chapter 1

## Introduction

### 1.1. Coherent light source

A laser is a device which emits optically amplified electromagnetic waves through a process of the stimulated emission, as read in its full name “Light Amplification by Stimulated Emission of Radiation”. A laser is a very unusual and interesting light source for its coherent characteristics. High spatial coherence can make a laser to be tightly focused into a tiny spot allowing the concentrating large light energy on a very small area. Also, the coherence enable a laser beam to propagate over great distance without much stray lights. Temporal coherence allows a laser to have a highly narrow spectrum.

After the first theories proposed by Albert Einstein [1] in 1917 for the coefficients for the absorption, spontaneous emission, stimulated emission of electromagnetic radiation, over 30 years had passed to experimentally obtain the first amplification and generation of electromagnetic waves by stimulated emission in microwave range. Nowadays, a variety of lasers in their structural and material composition are widely used in forms of commercial products. Besides consumer electronic devices like laser printers, optical disk drives, laser lighting displays, lasers are utilized in varied fields of interferometry, spectroscopy, imaging, lithography, metrology, communications, atomic cooling, material processing, and so on.

### 1.1.1. Semiconductor lasers

A semiconductor laser is a kind of lasers based on optical gain obtained by stimulated emission from an inter-band transition process on conditions of a high carrier density in the conduction band of semiconductor materials. With pumping energy into semiconductor materials, excited electrons on a higher states recombine the holes in the valence band emitting photons with an energy near bandgap energy. This recombination process can be stimulated by photons having adequate wavelength.

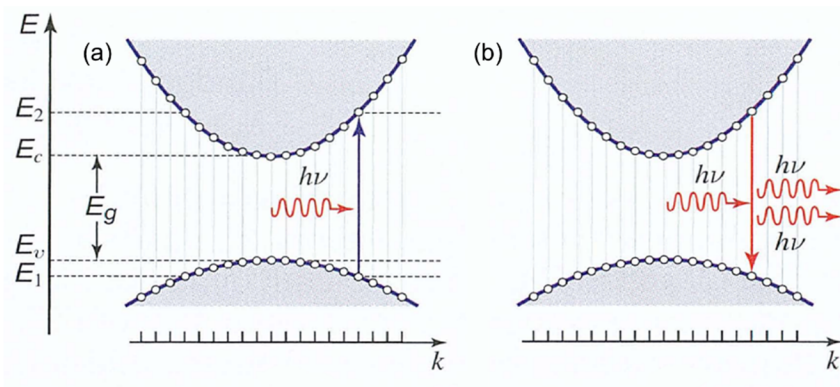


Figure 1-1-1 Absorption of a photon and generation of a stimulated photon [2].

Common semiconductor materials for lasing actions are three-five semiconductor materials with direct bandgap such as GaAs, GaN, InP, and their ternary and quaternary compounds. Direct bandgap material is an efficient light emitter because they do not need extra momentum for the charge carriers to recombine. The typical semiconductor lasers can be electrically pumped with moderate voltages and high efficiency and a wide range of wavelengths can be achieved for different devices from visible to mid-infrared. The fundamental advantage as compared to others such as gas- or solid-state lasers, comes from the direct current injection mechanism to provide population inversion allowing the lasers to be highly reliable, cheap and compact. Also, short upper-state lifetime of semiconductor lasers allows the device to be modulated with high frequencies, which leads to usefulness in optical communications, spectroscopy, etc.

Conventional semiconductor lasers also have some limitations in spite of many advantages. Due to the different lattice constants of semiconductor materials, substrate or epitaxial layers have to be carefully considered to obtain good quality of light-emitting devices. And the light source with different wavelengths are not easily compatible in one chip device. So the high density integration of a variety of photonic devices is hard to achieve. This demerit would be partially resolved in use of zero-dimensional colloidal type semiconductor materials as later chapters.

### 1.1.2. Laser source for high-density photonic integration

Since mankind has appeared in the world, there has not been a time when information is more abundant and its processing speed is faster than now. This is due not only to the increase in the number of human beings, but also to the development of electronics-based integrated circuits, computers, and communication technologies. Integrated circuits have been dazzlingly developed in the meantime, but it is true that they are approaching their physical limits. Although it is still in its infancy, it is necessary to pay attention to photonic integrated circuits having an alternative nature of the electronic integrated circuits. Photonic integrated circuits (PICs) are an implementation of various optical functions on a single chip, and uses lights as a medium for signal transmission. Lights have generally faster velocities than electrons and advantages in parallel processing by the superposition principle. Currently, the researches focus mainly on the materials based on InP or Si semiconductors, because it is efficient to fabricate light sources and passive devices. In particular, for the construction of a high-density PICs, realization of compact and efficient light sources is required. Vertical cavity surface emitting lasers, micro-disk lasers, photonic crystal (PhC) lasers, and plasmonic lasers have been studied. Among them, PhC lasers are one of promising sources because of their compactness, controllability of photonic modes, low-loss non-metal composition. In this thesis, PhC lasers are discussed further.

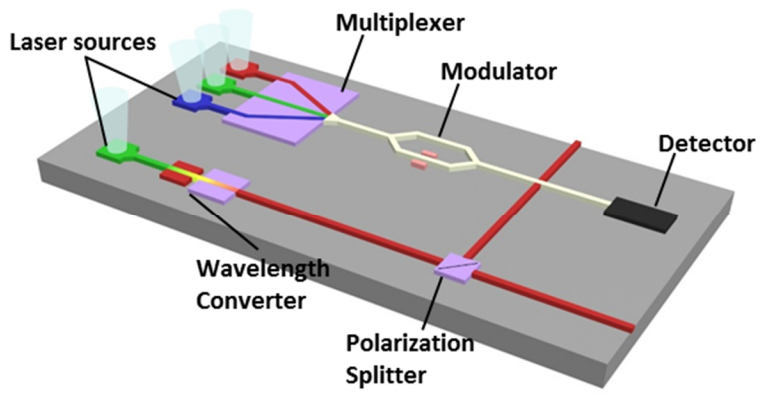


Figure 1-1-2 Conceptual image of PICs.

## 1.2. Photonic crystals

### 1.2.1. Introduction

The PhC is a periodic structure composed of two or more materials having different dielectric constants where a lattice constant is comparable to the wavelength of light. Schematic image of 1D, 2D, and 3D PhC structures is presented as Figure 1-2-1. One dimensional example of PhC is a quarter-wave stack [3]. The light of a specific wavelength incident on the quarter-wave stack structure can cause constructive or destructive interference of reflection waves at the interfaces of multilayer structure. Also, a plenty of optical devices have been developed since this principle was discovered by Lord Rayleigh in 1887 [4].

Higher dimensional cases of PhC structures were first introduced by E. Yablonovitch and S. John in 1987 [5,6]. In recent research area, 2D PhC slab is one of widely used structures because the 2D slab structure is advantageous to manufacturing the structure and manifesting the characteristics of PhC. In the slab design where the planar structure of high index materials is cladded by lower index materials, light is confined by total internal reflection in vertical direction. Also, periodic photonic structure allows band properties of the guided light in the horizontal direction.

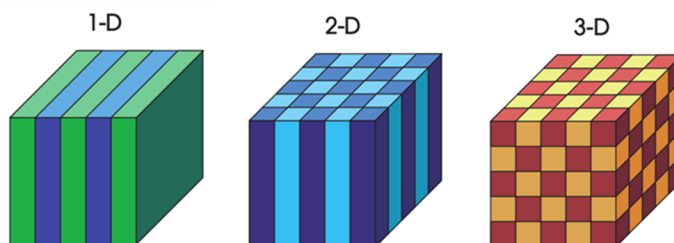


Figure 1-2-1 Examples of 1D, 2D, and 3D PhCs [7].

### 1.2.2. Photonic band structure

The electromagnetic waves passing through the PhC have an extraordinary photonic dispersion relation that cannot be found when the waves passing through a homogeneous medium. The exotic behavior of light in PhC can be understood from an analogy between photonics and electronics. The periodic potential of photons in the PhC has correspondence to the periodic potential of electrons in the semiconductor crystal [7,8]. In the semiconductor crystal, the periodic Coulomb interaction by the nucleus at each lattice site affects the states of electrons. Electronic band structures, the allowed energy states of electrons, can be derived by solving the Schrödinger equation. Similarly, the change in the periodic refractive index in PhC structure plays a role of the periodic potential in the photons. Also, allowed energy states of photons, photonic band structures can be derived by solving the Maxwell's equations for electromagnetic waves which propagate in the PhC. An example of photonic band structures of 2D hexagonal lattice PhC structure is illustrated as Figure 1-2-2.

In the semiconductor crystal, the electrons in a specific energy region are inhibited from proceeding in a specific direction due to the periodic potential of the atoms. Furthermore, the electrons are inhibited in any direction if the potential is large enough to cause a complete band-gap in which electrons of a specific energy region cannot exist in the semiconductor crystal. Likewise, in PhC, there exists photonic band-gap states where the photons of a certain frequency will not be able to propagate in any direction if the refractive index contrast is large enough. This phenomenon can be applied for PhC cavity and PhC waveguides. Another notable phenomenon in PhC arise at the Brillouin zone edge where the photons have near-zero group velocity. This band-edge phenomenon can be utilized to enhance the performance of photonic

devices like semiconductor laser and color converter, solar-cell, and so on.

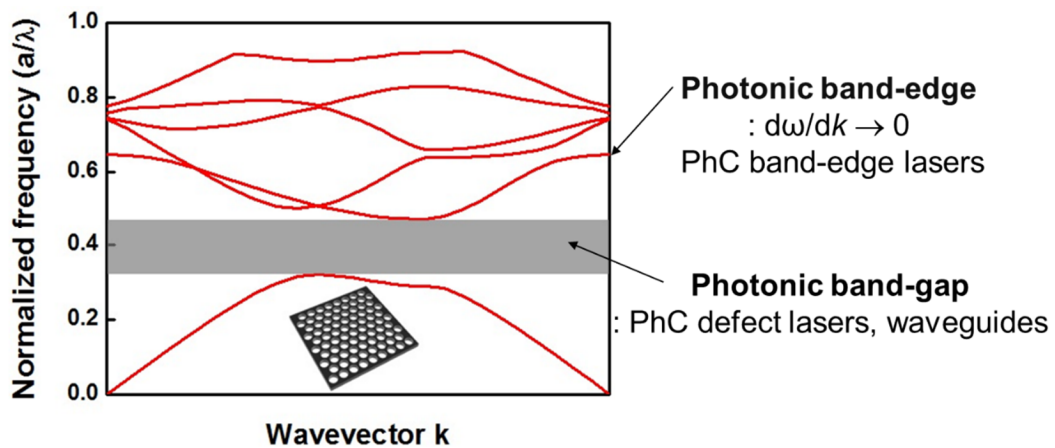


Fig. 1-2-2 Photonic band structure of a 2D hexagonal lattice PhC.

### 1.2.3. Photonic crystal band-edge laser

The interesting phenomenon at the Brillouin zone edge can be used for obtain a laser device. The slope of the dispersion relation or photonic band structure corresponds to the group velocity of the photons [8]. Generally, Brillouin zone edges in PhC have zero slope value, which means that there exists photonic states having zero group velocity. These states can be utilized for confining and amplifying the light energy as the J. P. Dowling first introduced so-called PhC band-edge lasers in 1994 [10]. Enhanced interaction between electromagnetic waves and gain materials at photonic band-edge allows the laser operations [9-11].

PhC band-edge lasers have extended cavity structures unlike the conventional lasers have definite mirrors which have high reflectivity. Thus, the PhC band-edge laser has several unique advantages. First, the PhC band-edge laser has a large alignment tolerance in fiber-coupling because it does not have a specific cavity structure [12,13]. It is also advantageous in that it can obtain higher output power than PhC cavity laser from the spatially extended mode [14]. Since the PhC band-edge laser structure has a periodic structure without a defect, it can be fabricated using an alternative lithography technique such as laser interference lithography [14] or nanosphere lithography [15] instead of conventional E-beam lithography. An example of 2D hexagonal lattice PhC band-edge laser is shown in Fig. 1-2-3. Furthermore, it is also possible to fabricate in-plane-emitting lasers using the Brillouin zone boundary band-edge point and to fabricate surface-emitting lasers using the Brillouin zone center band-edge point.

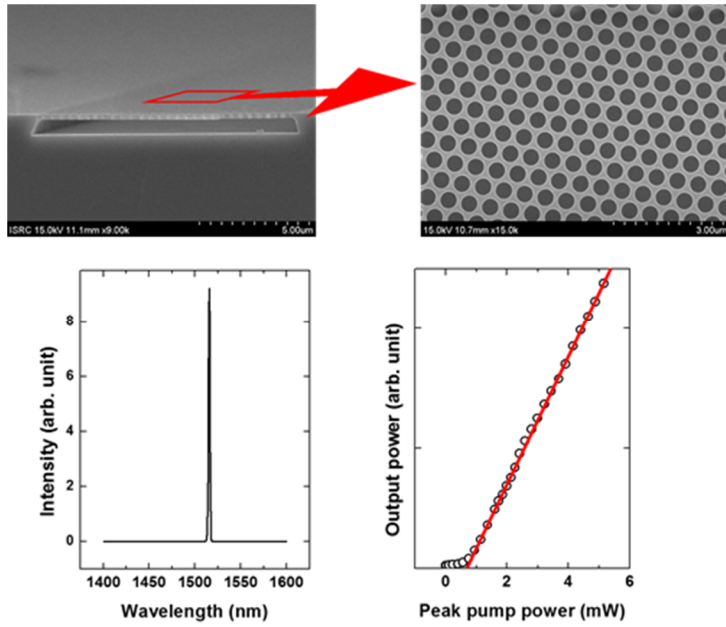


Figure 1-2-3 2D hexagonal lattice PhC band-edge laser [15].

#### 1.2.4. Photonic crystal cavity laser

Photonic band-gap states also can be utilized as a principle for confining and stimulating the light emission. While the PhC band-edge laser is mostly composed of perfectly periodic patterns, the PhC cavity laser have a defect structure in periodic patterns. The PhC cavity laser has a small spatial dimension, which is orders of wavelength of photons, and a very large Q-factor resulting in a very low laser threshold. The cavity size also can be designed to be small enough to support only a single mode which means that the laser can be controlled with high reliability.

Schematic of a square lattice PhC cavity laser structure is drawn in Fig. 1-2-4. The PhC cavity laser structure is formed of a periodic square-lattice PhC structure and a single defect. As shown in Fig. 1-2-4, the photons generated in the defect structure are confined laterally by the photonic band-gap and vertically by the total internal reflection due to the difference of the refractive index between the PhC slab and air-cladding. An example of a square lattice PhC cavity laser with a single defect is shown in Fig. 1-2-5.

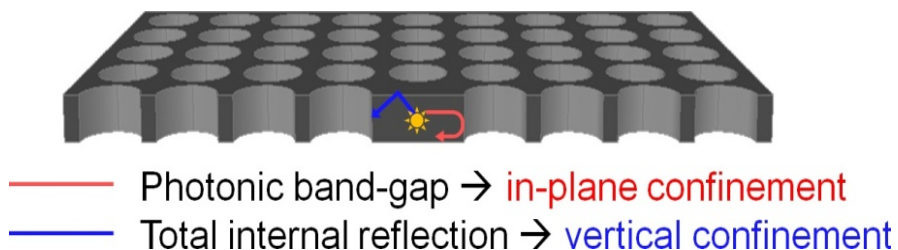


Figure 1-2-4 Schematic drawing of single-defect PhC cavity laser.

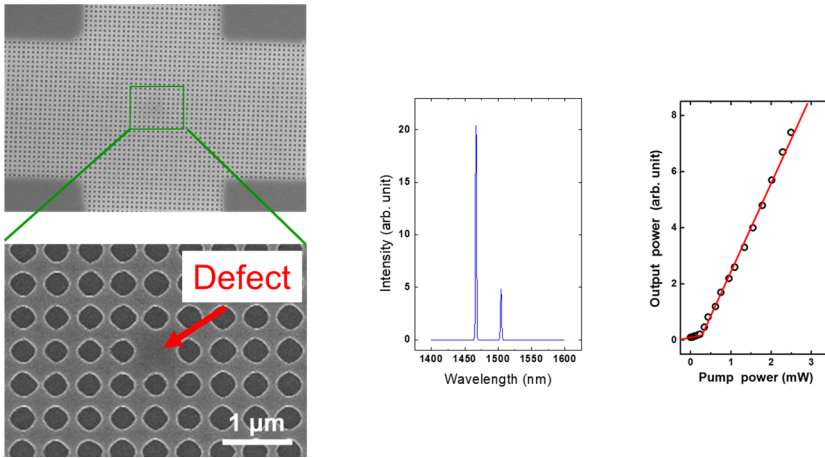


Figure 1-2-5 Single-defect PhC cavity laser [16].

### 1.3. Hybrid photonic crystal laser

Recently, hybrid PhC lasers, composed of a passive PhC backbone structure and an extrinsic optical gain material, have recently attracted much attention. They offer not only a cost-effective way of preparing compact lasers but also the freedom in choosing gain material from a variety of available ones, including (but not limited to) colloidal quantum dots (CQDs) [17–19], halide perovskites [20,21], transition metal dichalcogenides [22], organic dyes [23,24], or even biomaterials [25,26]. Hybrid PhC lasers can be one of promising coherent sources to realizing high density PICs.

An example of hybrid PhC band-edge laser is shown in Fig. 1-3-1. DFB laser composed of fused quartz grating backbone structure and solution-processed optically active halide perovskite alloy material is operated at  $T = 77$  K. Also, PhC cavity type laser made of GaP PhC L3 cavity passive structure and monolayer  $\text{WSe}_2$  as a gain material are presented as Fig. 1-3-2. Strongly confined electric fields in cavity structures interact the external gain materials resulting in stimulated emission.

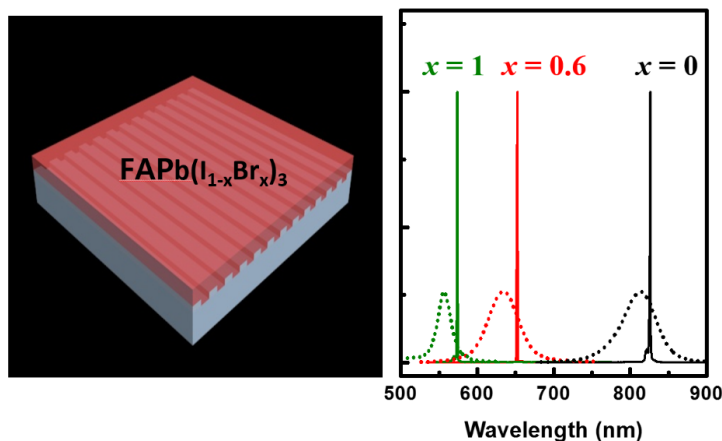


Figure 1-3-1 Hybrid PhC band-edge laser [27].

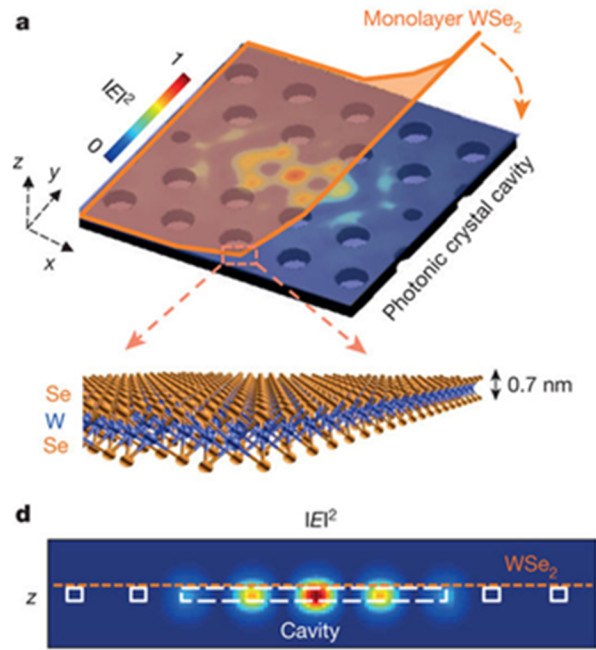


Figure 1-3-2 Hybrid PhC cavity laser [22].

### 1.3.1. Colloidal quantum dots as external gain materials

CQDs are a luminescent nanoscale material with many attractive and desirable properties, such as low-cost chemical synthesis in monodisperse size [28,29], and high luminous efficiency (QYs > 90%) [30]. Moreover, the CQD emission wavelength can be tuned simply by controlling its size during synthesis, yet without deteriorating the spectral purity and emission efficiency [31,32]. These unique advantages make CQDs ideal nano-building blocks to be used in a variety of applications, including display [33,34], lighting [35,36], and bio-sensing [37].

The CQDs acts as an external gain materials combined with the passive structural optical cavity structure in later chapters to obtain efficient hybrid PhC laser source. I used CdSe/CdS/ZnS CQDs in this study, of which structure is shown in Fig. 1-3-5. And the photoluminescence spectrum of red CQDs are displayed as Fig. 1-3-6. The CQDs spectrum have center wavelength of 615 nm and FWHM of 30 nm. Also, refractive index and extinction coefficient of spin-casted CQDs film are measured by ellipsometry method. CQDs have refractive index value of 1.77 near emission wavelengths.

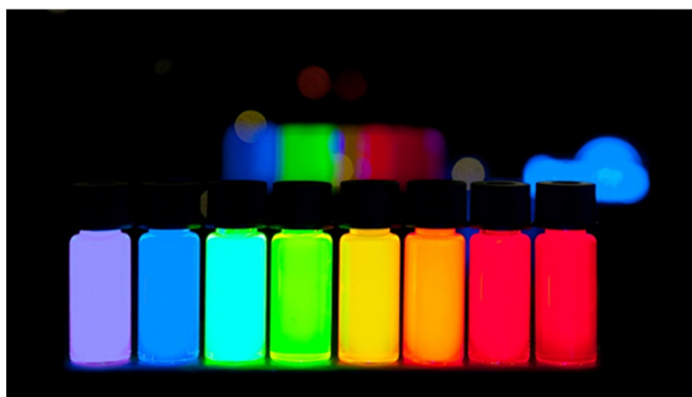


Figure 1-3-3 CQDs with different diameters exhibiting various colors [38].

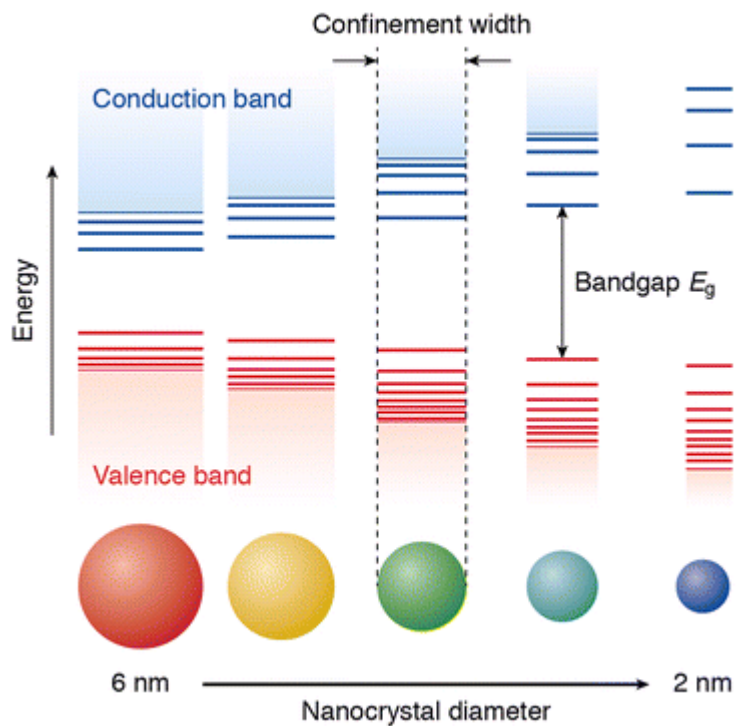


Figure 1-3-4 Schematic diagram of energy levels in CQDs [39].

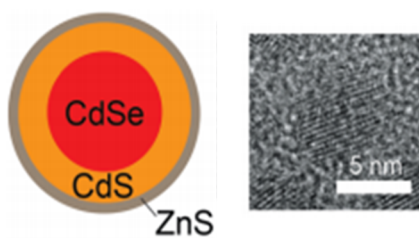


Figure 1-3-5 Structure of CdSe/CdS/ZnS CQDs.

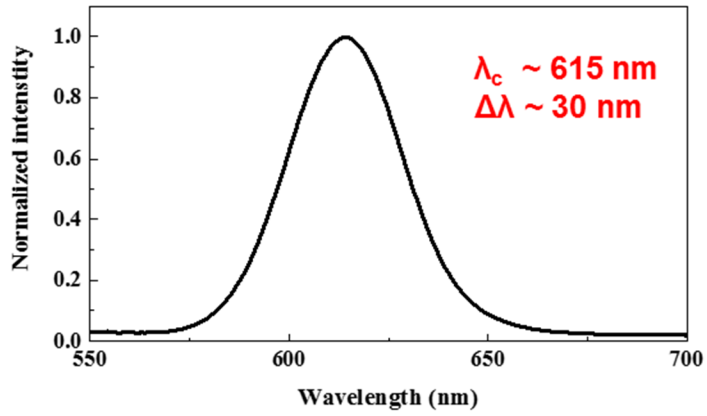


Figure 1-3-6 Photoluminescence emission spectrum of red CQDs.

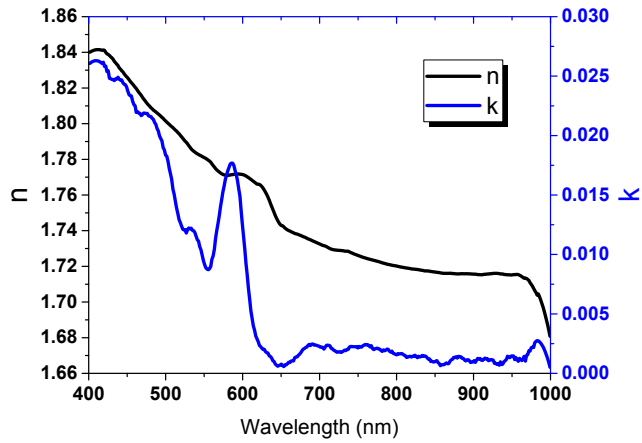


Figure 1-3-7 Complex refractive index of red CQDs.

## 1.4. Computational method

### 1.4.1. Plane wave expansion method

Plane wave expansion (PWE) method is a computational technique in electromagnetics that solves the eigenvalue problems of the Maxwell's equations. The solutions of the homogeneous Helmholtz equation are plane waves forming the basis for a periodic media. The PWE method is based on the Bloch theorem, the electric field (E-field) or magnetic field (H-field) can be expanded into appropriate Fourier series along their reciprocal lattice vector. Likewise, the dielectric permittivity is also expanded into the Fourier series. Then, these Fourier series equations replace infinite-dimensional matrix eigenvalue problems that can be solved with the appropriate approximation. PWE method is useful for calculating modal solutions of Maxwell's equations for inhomogeneity or periodic geometry and is commonly used for calculating the photonic band structure [40].

### 1.4.2. Finite-difference time-domain method

The finite difference time domain method (FDTD) is one of the most powerful computational methods for solving electromagnetic problems in the PhC research. Unlike the PWE method, FDTD methods solve the Maxwell's equations directly, and provide straightforward models for arbitrary structures. Furthermore, FDTD methods deal with the time-domain terms, so, it can cover a wide frequency band with a single simulation run. The FDTD method can be classified as a grid-based differential time-domain numerical modeling method [41]. Time-dependent Maxwell's equations are discretized to the space and time partial derivatives. The finite-difference equations are solved in a leap-frog manner. The vector components of the E-field in a volume of space are solved at a given instant in time; then the vector components of the H-field in the same spatial volume are solved at the next instant in time; and the process iterates repeatedly until the steady-state electromagnetic behavior is fully converged.

## 1.5. Outline of the manuscript

In this thesis, I introduced hybrid type PhC lasers, coherent light sources composed of a passive optical structure and external active gain materials. The external CQDs gain materials are combined with several passive backbone structure. The laser devices do functions for several applications.

In chapter 2, I will discuss about the efficient platform for on-chip integration of CQD PhC laser and passive components. Based on high index silicon nitride waveguide, conceptual PIC is experimentally demonstrated. PhC band-edge laser, slab waveguide, output coupler devices are integrated on a single chip.

In chapter 3, I will describe continuously tunable DFB laser device composed of CQD film on chirped grating. With modified Lloyd's LIL configurations, chirped gratings for tunable DFB laser source are efficiently fabricated over large area. After wet-transferring of CQDs onto grating, optical properties of the device are numerically & experimentally analyzed.

Finally, in chapter 4, the conclusion and the perspectives will be presented.

In appendix, bio-compatible silk DFB laser with physically transient characteristics are demonstrated. It is a bio-compatible version of hybrid PhC laser composed of silk, fused silica, dyes. The silk active can be easily removed and the laser device can be renewed repeatedly. More, chemosensing capability for detecting hydrochloride vapor using laser device are presented.

# References

- [1] A. Einstein, "Zur Quantentheorie der Strahlung," *Physikalische Zeitschrift* **18**, 121-128 (1917).
- [2] B.E.A. Saleh, M.C. Teich, *Fundamentals of Photonics* (Wiley 2007).
- [3] P. Yeh, *Optical Waves in Layered Media* (Wiley 2005).
- [4] J. W. Strutt (Lord Rayleigh), "On the maintenance of vibrations by forces of double frequency, and on the propagation of waves through a medium endowed with a periodic structure," *Philosophical Magazine Series* **5**, 145-159 (1887).
- [5] E. Yablonovitch, "Inhibited spontaneous emission in solid-state physics and electronics," *Physics Review Letters* **58**, 2059-2062 (1987).
- [6] S. John, "Strong localization of photons in certain disordered dielectric superlattices," *Physics Review Letters* **58**, 2486-2489 (1987).
- [7] J. D. Joannopoulos, S. G. Johnson, J. N. Winn, R. D. Meade, *Photonic Crystals: Molding the Flow of Light* (Princeton University Press 2008).
- [8] K. Inoue, K. Ohtaka, *Photonic Crystals: Physics, Fabrication and Applications* (Springer 2004).
- [9] J. P. Dowling, M. Scalora, M. J. Bloemer, C. M. Bowden, "The photonic band edge laser: A new approach to gain enhancement," *Journal of Applied Physics* **75**, 1896-1899 (1994).
- [10] S. Nojima, "Optical-gain enhancement in two-dimensional active photonic crystals," *Journal of Applied Physics* **90**, 545-551 (2001).
- [11] M. Imada, S. Noda, A. Chutinan, T. Tokuda, M. Murata, G. Sasaki, "Coherent two-dimensional lasing action in surface-emitting laser with triangular-lattice

- photonic crystal structure," *Applied Physics Letters* **75**, 316-318 (1999).
- [12] Y. Park, S. Kim, C. Moon, H. Jeon, H. J. Kim, "Butt-end fiber coupling to a surface-emitting  $\Gamma$ -point photonic crystal band edge laser," *Applied Physics Letters* **90**, 171115 (2007).
- [13] S. Kim, Y. Park, K. Hwang, J. Lee, H. Jeon, H. J. Kim, "High-power and large-alignment-tolerance fiber coupling of honeycomb-lattice photonic crystal  $\Gamma$ -point band-edge laser," *Journal of the Optical Society of America B* **26**, 1330-1333 (2009).
- [14] S. Kim, S. Ahn, J. Lee, H. Jeon, P. Regreny, C. Seassal, E. Augendre, L. D. Cioccio, "Milliwatt-level fiber-coupled laser power from photonic crystal band-edge laser," *Optics Express* **19**, 2105-2110 (2011).
- [15] S. Ahn, H. Kim, H. Jeon, J. Oh, Y. Do, H. Kim, "Two-dimensional hexagonal lattice photonic crystal band-edge laser patterned by nanosphere lithography," *Applied Physics Express* **5**, 042102 (2012).
- [16] S. Ahn, S. Kim, H. Jeon, "Single-defect photonic crystal cavity laser fabricated by a combination of laser holography and focused ion beam lithography," *Applied Physics Letters* **96**, 131101 (2010).
- [17] F. Fan, O. Voznyy, R. P. Sabatini, K. T. Bicanic, M. M. Adachi, J. R. McBride, K. R. Reid, Y.-S. Park, X. Li, A. Jain, R. Quintero-Bermudez, M. Saravanapavanantham, M. Liu, M. Korkusinski, P. Hawrylak, V. I. Klimov, S. J. Rosenthal, S. Hoogland, E. H. Sargent, "Continuous-wave lasing in colloidal quantum dot solids enabled by facet-selective epitaxy," *Nature* **544**, 75–79 (2017).
- [18] C. Dang, J. Lee, C. Breen, J. S. Steckel, S. Coe-Sullivan, A. Nurmikko, "Red, green and blue lasing enabled by single-exciton gain in colloidal quantum dot films," *Nature Nanotechnology* **7**, 335–339 (2012).

- [19] C. Dang, J. Lee, K. Roh, H. Kim, S. Ahn, H. Jeon, C. Breen, J. S. Steckel, S. Coe-Sullivan, A. Nurmikko, "Highly efficient, spatially coherent distributed feedback lasers from dense colloidal quantum dot films," *Applied Physics Letters* **103**, 171104 (2013).
- [20] S. Chen, K. Roh, J. Lee, W. K. Chong, Y. Lu, N. Mathews, T. C. Sum, A. Nurmikko, "A photonic crystal laser from solution based organo-lead iodide perovskite thin films," *ACS Nano* **10**, 3959–3967 (2016).
- [21] M. Saliba, S. M. Wood, J. B. Patel, P. K. Nayak, J. Huang, J. A. Alexander-Webber, B. Wenger, S. D. Stranks, M. T. Hörantner, J. T.-W. Wang, R. J. Nicholas, L. M. Herz, M. B. Johnston, S. M. Morris, H. J. Snaith, M. K. Riede, "Structured organic–inorganic perovskite toward a distributed feedback laser," *Advanced Materials* **28**, 923–929 (2015).
- [22] S. Wu, S. Buckley, J. R. Schaibley, L. Feng, J. Yan, D. G. Mandrus, F. Hatami, W. Yao, J. Vučković, A. Majumdar, X. Xu, "Monolayer semiconductor nanocavity lasers with ultralow thresholds," *Nature* **520**, 69–72 (2015).
- [23] S. Toffanin, S. Kim, S. Cavallini, M. Natali, V. Benfenati, J. J. Amsden, D. L. Kaplan, R. Zamboni, M. Muccini, F. G. Omenetto, "Low-threshold blue lasing from silk fibroin thin films," *Applied Physics Letters* **101**, 091110 (2012).
- [24] Z. Li, Z. Zhang, T. Emery, A. Scherer, D. Psaltis, "Single mode optofluidic distributed feedback dye laser," *Optics Express* **14**, 696–701 (2006).
- [25] M. C. Gather, S. H. Yun, "Single-cell biological lasers," *Nature Photonics* **5**, 406–410 (2011).
- [26] C. Vannahme, F. Maier-Flaig, U. Lemmer, A. Kristensen, "Single-mode biological distributed feedback laser," *Lab on a Chip* **13**, 2675–2678 (2013).

- [27] H. Cha, S. Bae, H. Jung, M. J. Ko, H. Jeon, "Single-mode distributed feedback laser operation in solution-processed halide perovskite alloy system," *Advanced Optical Materials* **5**, 042102 (2017).
- [28] O. Chen, J. Zhao, V. P. Chauhan, J. Cui, C. Wong, D. K. Harris, H. Wei, H.-S. Han, D. Fukumura, R. K. Jain, M. G. Bawendi, "Compact high-quality CdSe–CdS core–shell nanocrystals with narrow emission linewidths and suppressed blinking," *Nature Materials* **12**, 445-451 (2013).
- [29] C. Murray, D. J. Norris, M. G. Bawendi, "Synthesis and characterization of nearly monodisperse CdE (E= sulfur, selenium, tellurium) semiconductor nanocrystallites," *Journal of the American Chemical Society* **115**, 8706-8715 (1993).
- [30] R. Rossetti, S. Nakahara, L. E. Brus, "Quantum size effects in the redox potentials, resonance Raman spectra, and electronic spectra of CdS crystallites in aqueous solution," *The Journal of Chemical Physics* **79**, 1086-1088 (1983).
- [31] A. P. Alivisatos, "Semiconductor clusters, nanocrystals, and quantum dots," *Science* **271**, 933-937 (1996).
- [32] J. Y. Kim, O. Voznyy, D. Zhitomirsky, E. H. Sargent, "25th anniversary article: Colloidal quantum dot materials and devices: A quarter-century of advances," *Advanced Materials* **25**, 4986-5010 (2013).
- [33] E. Jang, S. Jun, H. Jang, J. Lim, B. Kim, Y. Kim, "White-light-emitting diodes with quantum dot color converters for display backlights," *Advanced Materials* **22**, 3076-3080 (2010).
- [34] T.-H. Kim, K.-S. Cho, E. K. Lee, S. J. Lee, J. Chae, J. W. Kim, D. H.

- Kim, J.-Y Kwon, G. Amaratunga, S. Y. Lee, B. L. Choi, Y. Kuk, J. M. Kim, K. Kim, “Full-colour quantum dot displays fabricated by transfer printing,” *Nature Photonics* **5**, 176 (2011).
- [35] V. L. Colvin, M. C. Schlamp, A. P. Alivisatos, “Light-emitting diodes made from cadmium selenide nanocrystals and a semiconducting polymer,” *Nature* **370**, 354 (1994).
- [36] Y. Shirasaki, G. J. Supran, M. G. Bawendi, V. Bulović, “Emergence of colloidal quantum-dot light-emitting technologies,” *Nature Photonics* **7**, 13 (2013).
- [37] X. Michalet, F. F. Pinaud, L. A. Bentolila, J. M. Tsay, S. Doose, J. J. Li, G. Sundaresan, A. M. Wu, S. S. Gambhir, S. Weiss, “Quantum dots for live cells, in vivo imaging, and diagnostics,” *Science* **307**, 538-544 (2005).
- [38] N. C. Anheier, “Colorful particles for spectrometry,” *Nature* **523**, 39-40 (2015).
- [39] F. T. Rabouw, C. de Mello Donega, *Excited-State Dynamics in Colloidal Semiconductor Nanocrystals* (Springer 2017).
- [40] S. Shi, C. Chen, and D. W. Prather, “Plane-wave expansion method for calculating band structures of photonic crystal slabs with perfectly matched layers,” *Journal of the Optical Society of America A* **21**, 1769-1775 (2004)
- [41] K. S. Yee, “Problems involving Maxwell’s equations in isotropic media,” *IEEE Transactions on Antennas and Propagation* **14**, 802-807 (1966)



## Chapter 2

# Efficient platform for on-chip integration of colloidal quantum dot photonic crystal band-edge laser based on silicon nitride waveguide

### 2.1. Introduction

Lasers based on the resonance principles of PhCs have been studied actively because of their small sizes and low power consumption [1–7], the virtues for compact light sources to be used in future high-density PICs. In particular, hybrid PhC lasers, composed of a passive PhC backbone structure and an extrinsic optical gain material, have recently attracted much attention. Interestingly, the hybrid PhC lasers still offer a unique structural advantage that other types of regular or PhC laser structures cannot. By limiting the spatial area for a PhC laser (in terms of both PhC pattern and optical gain material), one can easily distinguish the zones for active and passive devices. Furthermore, a high optical coupling efficiency between them is automatically guaranteed because they share the same coplanar backbone waveguide layer. This not only facilitates the integration of a PhC laser and a passive waveguide, but also makes its extension to a large-scale PIC conceivable. This scheme is

distinguished from the previously reported ones that require enormous efforts in the alignment between different nanoscale/submicron structures [8,9]. In this study, I demonstrate a simple conceptual PIC, in which a hybrid PhC band-edge laser, a slab waveguide, and output couplers are all integrated on a single chip. Upon optical excitation, coherent single-mode laser output is emitted with well-defined in-plane emission directions, and subsequently coupled into the adjacent passive waveguide layer with a guaranteed high coupling efficiency. The coupled laser light propagates through the slab waveguide and is eventually out-coupled into free space through remote grating couplers. To vividly demonstrate directional in-plane emission from a PhC band-edge laser and also the controllability on it, here I intentionally employ a simple slab waveguide structure with no lateral confinement feature. Coupled laser light then propagates freely within the waveguide section but along the directions designated to the band-edge mode.

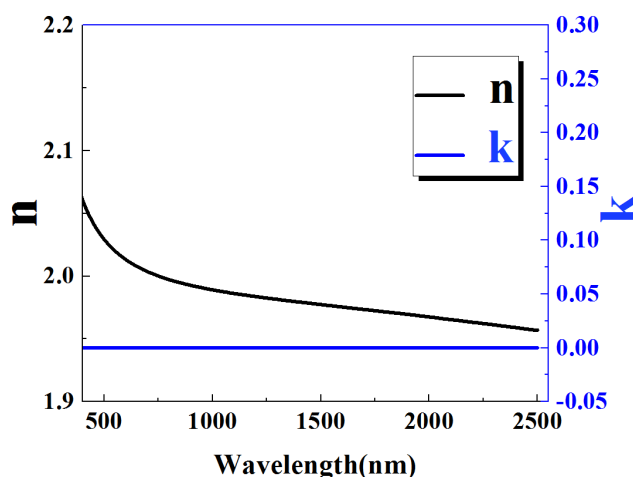


Figure 2-1-1 Complex refractive index of a silicon nitride film.

## 2.2. Device design and calculation

### 2.2.1. Photonic integration of active and passive devices

Fig. 2-2-1 shows a schematic of our device structure. Constructed in a single passive waveguide layer are a PhC pattern (for the formation of the band-edge laser), a waveguide section (with no specific waveguide pattern in the lateral direction), and a grating coupler. I choose silicon nitride ( $\text{Si}_3\text{N}_4$ ;  $n = 2.01$ ) and fused silica ( $\text{SiO}_2$ ;  $n = 1.46$ ) as the backbone waveguide layer and substrate, respectively, because of the high refractive index contrast and very low absorption in the visible to near-infrared wavelength range. Thus the  $\text{Si}_3\text{N}_4$  thin-film layer constitutes an asymmetric slab waveguide, clad by air above and the silica substrate below. The thickness of the  $\text{Si}_3\text{N}_4$  slab waveguide is designed to support only the fundamental guided mode in the vertical direction. Engraved into the  $\text{Si}_3\text{N}_4$  backbone layer are a 2D PhC air-hole array for a PhC band-edge laser and grating boxes for output couplers. Densely packed CQDs are then selectively deposited directly on top of the PhC pattern to provide optical gain for stimulated emission in red ( $\lambda \sim 615$  nm). A band-edge laser fabricated as such offers a continuous coupling interface to the adjacent passive waveguide section, which is composed of the  $\text{Si}_3\text{N}_4$  layer itself (with neither structural pattern nor CQDs atop).

Fig. 2-2-2 shows the refractive index profiles of the two sections and the corresponding transverse electric (TE) guided mode profiles, which visually demonstrate a high degree of mode match. For the refractive index of the CQD-capped PhC laser section, I take the geometrical average of the refractive indices of the two materials, CQDs and  $\text{Si}_3\text{N}_4$ . Simple mode overlap integration indicates that the butt coupling efficiency [10] between the two sections can be as high as  $\Gamma \approx 95\%$ .

Coupling efficiency at an abrupt interface between two waveguides can be roughly estimated by the overlap integral  $\eta = \eta_F \frac{|\iint E_{in}(y,z)E_{out}^*(y,z)dydz|^2}{\iint |E_{in}(y,z)|^2 dydz \iint |E_{out}(y,z)|^2 dydz}$ , where  $\eta_F = \frac{4n_{in} n_{out}}{(n_{in} + n_{out})^2}$ . For confirmation, I also perform FDTD simulations using commercial software (FDTD Solution, Lumerical Solutions). Fig. 2-2-3 shows the simulated guided mode profile ( $E_y$ ) near the joint between the PhC and the waveguide sections, which is obtained by launching from the left the fundamental guided mode supported by the PhC laser structure. The mode is guided well except for a small perturbation at the joint; consequently, most of the incident power ( $\sim 0.955$ ) is transmitted through the joint. A similar FDTD simulation is performed for the grating out-coupler. As shown in Fig. 2-2-3, a significant amount of the electromagnetic energy flux of the waveguide mode is coupled out into free space within the coupler section, which is composed of a second-order grating.

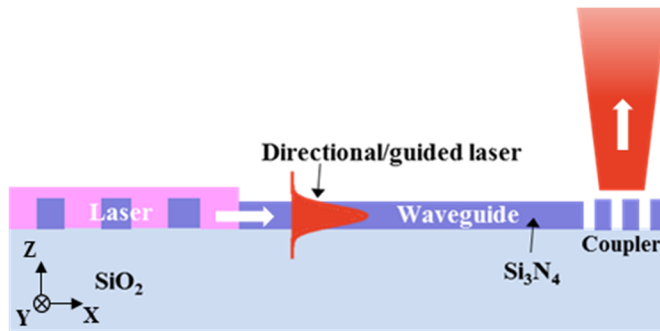


Figure 2-2-1 Schematic of on-chip integration of PhC band-edge laser, waveguide, and output coupler.

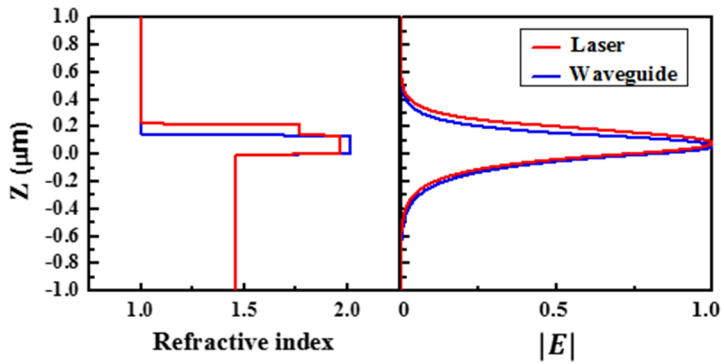


Figure 2-2-2 Refractive index profiles (left) and fundamental TE-guided mode profiles (right) of the CQD–PhC band-edge laser section (red) and  $\text{Si}_3\text{N}_4$  waveguide section (blue) at a wavelength of 615 nm.

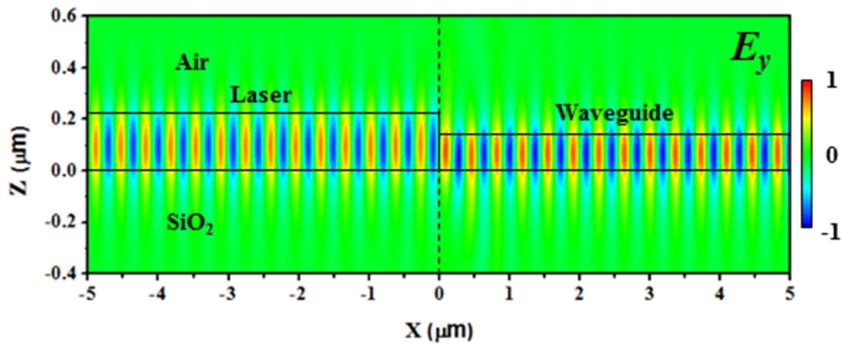


Figure 2-2-3 FDTD-simulated TE-guided mode propagation across the interface between the CQD–PhC laser structure and the  $\text{Si}_3\text{N}_4$  waveguide.

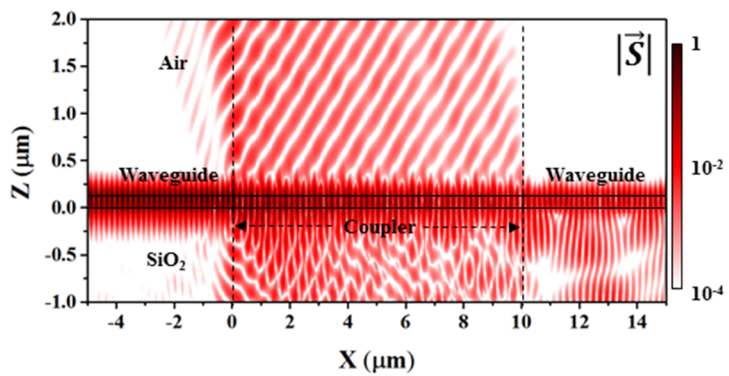


Figure 2-2-4 FDTD simulation near the joint between the waveguide and the grating coupler. The magnitude of the Poynting vector is plotted on a logarithmic scale.

### 2.2.2. Photonic band structure of colloidal quantum dots photonic crystal laser

Fig. 2-2-5 shows the photonic band structure of our 2D PhC band-edge laser structure for TE polarization, which is calculated using the 2D plane-wave expansion method. The PhC model structure is composed of a square-lattice array of air-holes that is etched into the  $\text{Si}_3\text{N}_4$  PhC backbone layer ( $t = 140$  nm) and overcoated with CQDs. The refractive index of the densely packed CdSe–CdS–ZnS core-shell-shell CQDs was obtained from spectroscopic ellipsometry measurements of an independently prepared film. It is well known that the photon group velocity at a band-edge mode vanishes ( $v_g = d\omega/dk = 0$ ) and that the optical gain is then effectively enhanced, enabling lasing action [11]. I use the X- or M-point band-edge modes below the light lines—marked by circles in Fig. 2-2-5—because they can afford in-plane lasing action with well-defined emission directions [12,13], which is suitable for on-chip integration with other photonic components.

Fig. 2-2-6 is simulated mode spectra for PhC lattice constants of  $a = 185$  and  $255$  nm, respectively, where the air-hole radius is fixed at  $r = 0.26a$ . The two lattice constants correspond to the conditions under which the X- and M-point band-edge modes, respectively, coincide with the red emission band of the CQDs used in this study ( $\lambda_c \sim 615$  nm;  $\Delta\lambda_{\text{FWHM}} \sim 32$  nm). The simulations are performed using the three-dimensional FDTD method with periodic boundary conditions. Each case exhibits two major distinct modes ( $M_1$  and  $M_2$  are narrowly spaced nondegenerate modes), which correspond to two neighboring band-edge modes, one belonging to the air band and the other to the dielectric band. The insets show simulated mode profiles; each image displays the in-plane electric field intensity ( $E_t^2 = E_x^2 + E_y^2$ ) at the center plane of the  $\text{Si}_3\text{N}_4$  backbone layer. The two sets of X-point band-edge modes are expected

to have in-plane momenta along the square Bravais lattice vectors, which is exactly what I see from the mode profiles in the insets of Fig. 2-2-6. The difference between them is the relative positions of the nodes and antinodes: the  $X_1/X_2$  modes (belonging to the dielectric band) have antinodes in the  $\text{Si}_3\text{N}_4$  dielectric region, whereas those of the  $X_3/X_4$  modes (belonging to the air band) run through the air-holes. Therefore, the  $X_3/X_4$  modes have greater overlap with the CQDs and thus are likely to lase; according to our evaluation, the CQD overlap factors are 37.1% for  $X_3/X_4$  and 5.9% for  $X_1/X_2$ . Similar arguments can be made for the M-point band-edges modes (except that their in-plane momenta are along the diagonal directions of the square lattice); the  $M_3/M_4$  modes, which belong to the air band, have a much higher modal overlap with the CQDs (25.7%) than the dielectric band-edge modes do (6.6% for  $M_1$  and 8.4% for  $M_2$ ), and thus have a better chance of lasing.

In order to investigate the overall modal behavior (including both mode generation and propagation), 2D FDTD simulations are performed for an extended area that includes the regions of not only the square lattice PhC but also a part of the planar waveguide. To facilitate the simulations, the refractive index contrast between the two materials is increased to 2 (instead of  $\sim 0.23$ ) while the width of the PhC region is reduced to  $3.5 \mu\text{m}$  (instead of  $50 \mu\text{m}$ ). Fig. 2-2-7 vividly shows not only the stable PhC band-edge modes in the center but also their subsequent propagation in the appropriate directions.

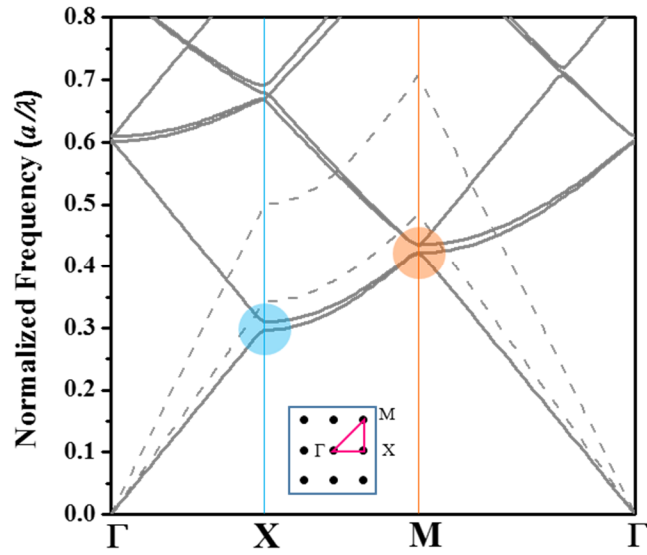


Figure 2-2-5 Photonic band structure of the 2D square-lattice PhC calculated by the plane-wave expansion method. The dashed lines represent the light lines in vacuum (upper) and in silica (lower).

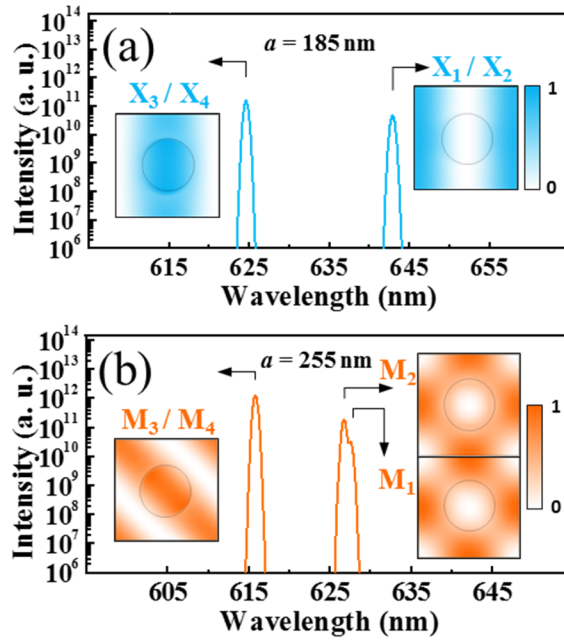


Figure 2-2-6 Resonant mode spectra calculated for the (a) X and (b) M symmetry points. The insets show the FDTD-calculated band-edge mode profiles within a unit cell.

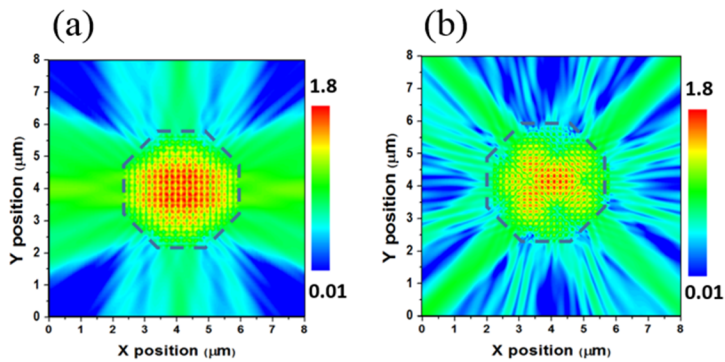


Figure 2-2-7 FDTD-simulated propagation of band-edge mode. Profile of electric field magnitude at (a) X-point ( $X_3/X_4$ ) and at (b) M-point ( $M_3/M_4$ ).

## 2.3. Device fabrication

To make real devices, I first prepared a clean fused silica substrate. A  $\text{Si}_3\text{N}_4$  thin film was deposited on the substrate by plasma-enhanced chemical vapor deposition to a nominal thickness of 140 nm. An array of simple PIC patterns was then defined using electron-beam lithography. Each PIC pattern contained a PhC laser in the center and eight grating couplers surrounding the PhC laser but away from it, as shown in Fig. 2-3-1 (a). The electron-beam resist patterns were then transferred to the underlying  $\text{Si}_3\text{N}_4$  layer by reactive-ion etching. The PhC laser pattern (50  $\mu\text{m}$  in width) was selectively covered with a CQD layer (80 nm in thickness) by lifting off the CQD layer after spin-coating it from solution (2.1 wt% in cyclohexane; 1000 rpm). The eight grating coupler boxes (each 10  $\mu\text{m}$   $\times$  30  $\mu\text{m}$  in size) face the eight side edges of the central octagon, with a slab waveguide region in between (50  $\mu\text{m}$  in length). I did not define any lateral confinement structure in this slab waveguide so that I could attempt to confirm directional emission and propagation of the band-edge laser beams by observing selective lighting of the grating boxes located in the corresponding directions. Fig. 2-3-1 (b) and (c) are scanning electron microscope (SEM) images of the PhC laser pattern ( $a = 255$  nm) and grating regions ( $\Lambda = 310$  nm; fill factor =  $\sim 0.65$ ), respectively, before selective CQD coating, and Figs. 2-3-1 (d) and (e) are tilted SEM images of the 2D PhC region (after CQD lift-off) and a grating coupler box, respectively. Figs. 2-3-1 (d) and its inset clearly demonstrate that CQDs not only cover the PhC-patterned area but also fill the air-holes uniformly.

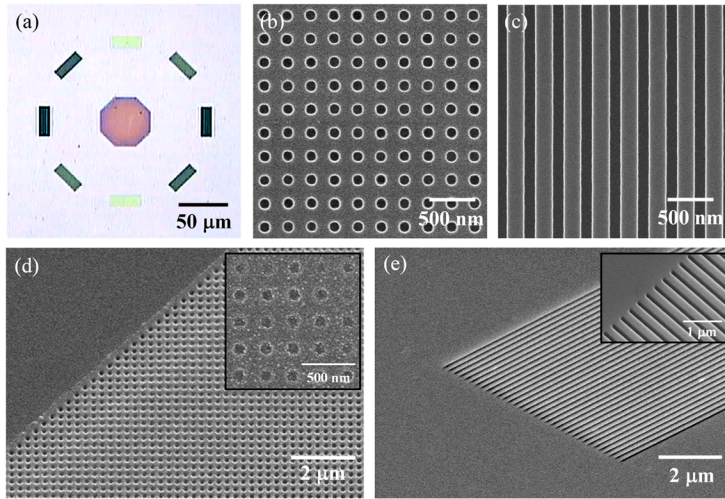


Figure 2-3-1 Device images. (a) Optical microscope image of one unit of fully fabricated device structure. An octagonal CQD–PhC laser (center) and eight grating couplers are integrated with a pattern-free region of  $\text{Si}_3\text{N}_4$  waveguide in between. A linear polarizer filter is inserted to differentiate the images of the output couplers depending on the orientation of the one-dimensional (1D) grating. (b), (c) SEM images taken from the top of (b) the  $a = 255$  nm PhC laser (before CQD deposition) and (c) the 1D grating coupler. (d), (e) Tilted SEM images of (d) the boundary between the CQD–PhC laser and the bare  $\text{Si}_3\text{N}_4$  waveguide and (e) the grating coupler. Insets show amplified SEM images of (d) the CQD–PhC laser section (top view after CQD deposition) and (e) the grating coupler (tilted view)

## 2.4. Optical measurements and analyses

### 2.4.1. Optical measurements set-up

I measured the microphotoluminescence of the fabricated PIC devices. Each device was optically activated using a frequency-doubled Nd:YAG laser ( $\lambda_{\text{ex}} = 532$  nm) at room temperature. I operated the laser in a pulsed mode at a low duty cycle (400 ps pulse width and 1 kHz repetition rate) to minimize the possibility of thermal damage. The excitation beam was focused downward onto the PhC band-edge laser with a spot size slightly larger than the octagonal PhC pattern using a 5 $\times$  objective lens (N.A. = 0.12). The PhC laser emission was captured from the top using the same objective lens and fed into a spectrometer (DW700, DongWoo Optron) for analysis.

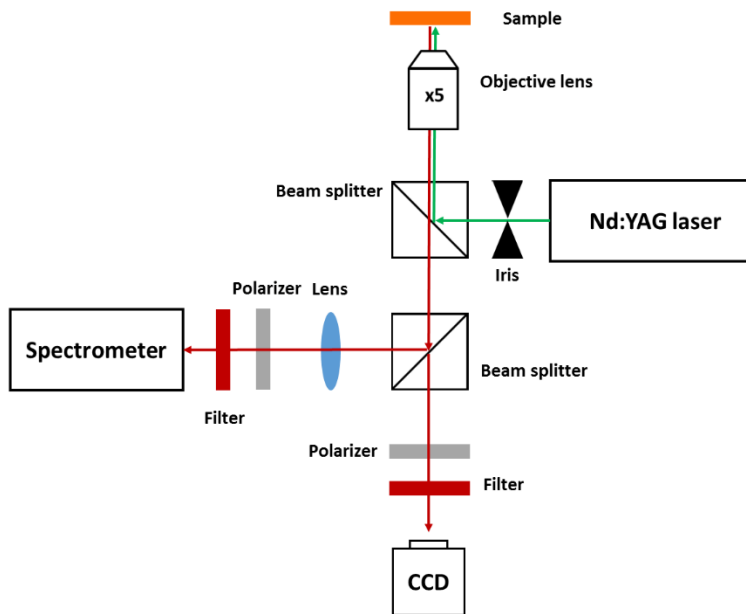


Figure 2-4-1 Schematically illustrated micro-PL setup

### 2.4.2. Laser emission properties of two symmetric points

Fig. 2-4-2 (a) shows emission spectra from the  $a = 185$  nm sample recorded at a few different excitation powers. Single-mode laser emission at  $\lambda \approx 624$  nm is clearly seen with a threshold pulse energy density of  $\sim 1$  mJ/cm<sup>2</sup> [Fig. Figure 2-4-2 (b)]. Figs. 2-4-4 (a), (b) are sample images taken with a charge-coupled device (CCD) camera while the device was optically excited below and above the laser threshold, respectively. A notch filter was installed in front of the CCD camera to eliminate scattered and stray light from the 532 nm excitation beam. Below the laser threshold, the device exhibits faint but uniform emission only from the QD-coated PhC region, which is characteristic of spontaneous emission. In contrast, however, the emission image changes dramatically above the threshold; it becomes much brighter and exhibits vivid speckle patterns indicative of lasing. One can clearly see not only the difference between the emission resulting from excitation below and above the threshold (in terms of the emission spectral widths). More importantly, there is additional emission from the four grating boxes located on the x and y axes. This is strong evidence that lasing occurs at the X-point band-edge modes, which is consistent with the fact that this PhC structure ( $a = 185$  nm) is designed to operate at these modes. The experimental CCD image shown in Figs. 2-4-4 (b) is consistent with a numerical simulation result Fig. 2-2-7 based on the 2D FDTD method. Similar arguments can be made for the  $a = 255$  nm sample, which is designed for M-point band-edge lasing.

Figure 2-4-3 (a) shows emission spectra captured at various excitation levels. Again, sharp single-mode laser emission ( $\lambda \approx 616$  nm) is obtained over a wide range of excitation pulse energy densities. The laser threshold ( $\sim 2$  mJ/cm<sup>2</sup>) is about twice that of the X-point band-edge laser, as shown in Figure 2-4-3 (b), which I attribute to

a lower Q factor and a smaller modal overlap with the gain volume for the M-point band-edge mode. Whereas the excited CQD–PhC area glows dimly below the threshold [Fig. 2-4-5 (a)], intense emission occurs with distinct speckle patterns not only from the CQD–PhC region but also from the grating couplers located at the four corners (in the diagonal directions) [Fig. 2-4-5 (b)]. This is a direct indication that lasing indeed occurs at the M-point band-edge modes, which is also supported by the FDTD simulation result for these modes.

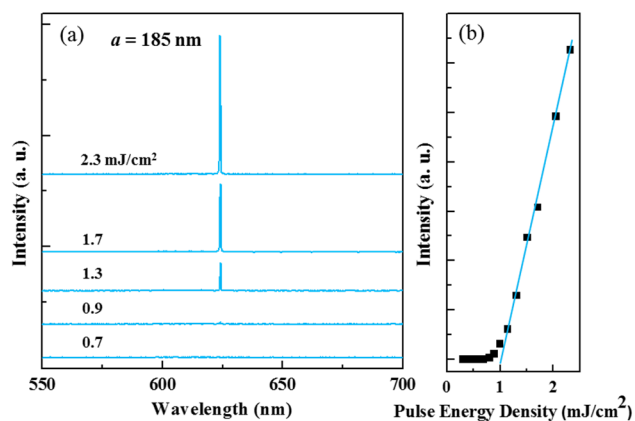


Figure 2-4-2 Emission properties of the CQD–PhC X-point band-edge laser. (a) Photoluminescence spectra at various excitation pulse energies. (b) Light input versus light output relationship.

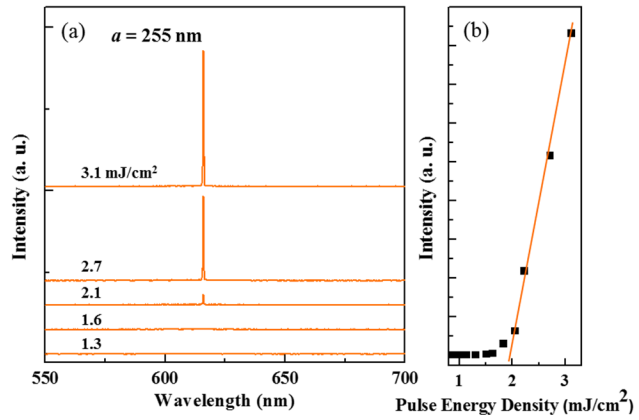


Figure 2-4-3 Emission properties of the CQD-PhC M-point band-edge laser. (a) Photoluminescence spectra at various excitation pulse energies. (b) Light input versus light output relationship.

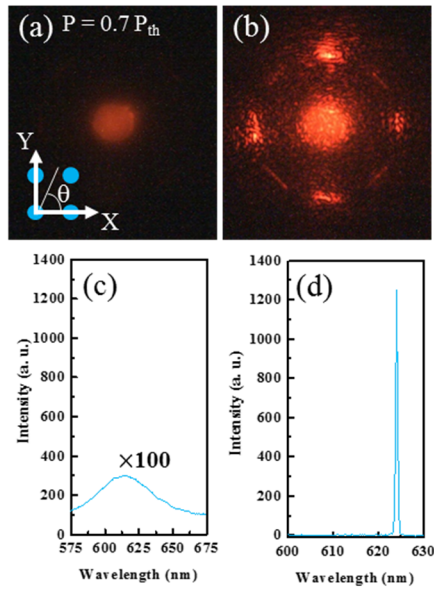


Figure 2-4-4 Emission properties of the CQD-PhC X-point band-edge laser. (a) CCD image of below laser threshold. (b) CCD image of above laser threshold (c) Emission spectrum of the device under optical excitation below laser threshold. (d) Emission spectrum of the device under optical excitation above laser threshold.

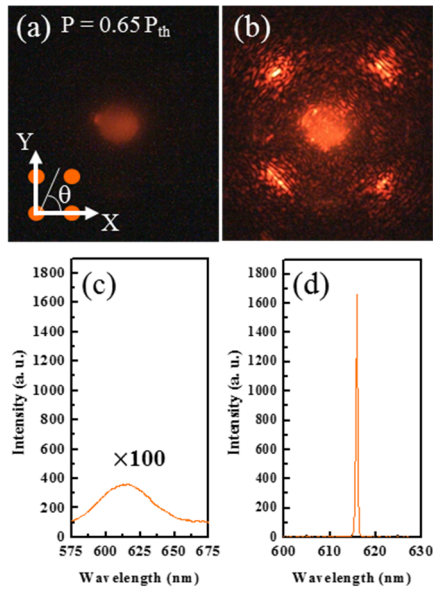


Figure 2-4-5 Emission properties of the CQD-PhC M-point band-edge laser. (a) CCD image of below laser threshold. (b) CCD image of above laser threshold (c) Emission spectrum of the device under optical excitation below laser threshold. (d) Emission spectrum of the device under optical excitation above laser threshold.

### 2.4.3. Polarization dependence of laser emission

The characteristics of the X-point band-edge lasing can be assessed further by examining its polarization dependence, which can be done by inserting linear polarizers into our microphotoluminescence setup. Figure 2-4-6 (a) and (b) are emission images taken when the polarizer angle is set to  $\theta = 0^\circ$  and  $90^\circ$ , respectively. When  $\theta = 0^\circ$  ( $90^\circ$ ) [or the electric field is along the x (y) axis], only the band-edge mode oscillating in the y (x) direction is visible. This observation implies that I could discriminate the two degenerate X-point band-edge modes (presumably  $X_3/X_4$ ) whose oscillation directions are orthogonal to each other and see the contributions of the two degenerate band-edge modes to the total emission intensity.

The polarization dependence of the laser emission patterns shown in Figure 2-4-7 (a) and (b) reveals that the M-point lasing is composed of two orthogonally degenerate modes. I assume that lasing occurs at the  $M_3/M_4$  modes because our CQD–PhC hybrid laser platform prefers the band-edge modes in the air band to those in the dielectric band (owing to a higher modal overlap factor with the CQD gain material). The emission spectra shown in Figure 2-4-7 (c), (d) confirm the lasing action and contributions of the two degenerate band-edge modes.

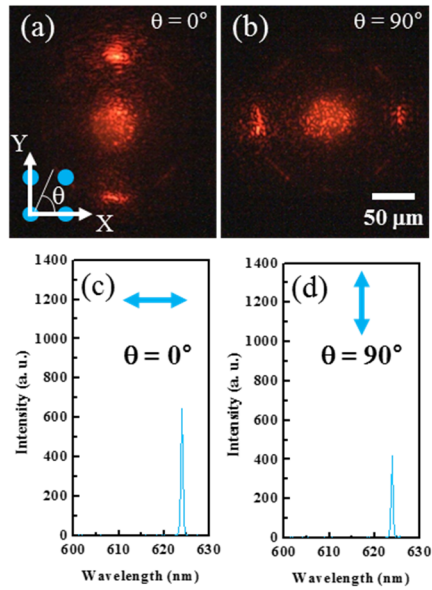


Figure 2-4-6 Polarized emission properties of the X-point sample above threshold (a) CCD image at  $0^\circ$  polarization angle (b) CCD image at  $90^\circ$  polarization angle (c) Emission spectrum of the device at  $0^\circ$  polarization angle (d) Emission spectrum of the device at  $90^\circ$  polarization angle.

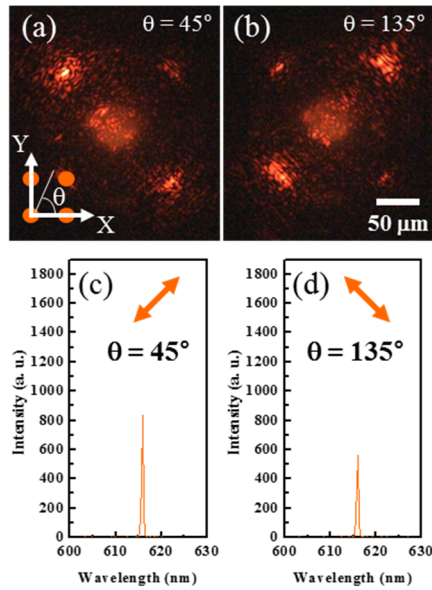


Figure 2-4-7 Polarized emission properties of the M-point sample above threshold (a) CCD image at  $45^\circ$  polarization angle (b) CCD image at  $135^\circ$  polarization angle (c) Emission spectrum of the device at  $45^\circ$  polarization angle (d) Emission spectrum of the device at  $135^\circ$  polarization angle

## 2.5. Summary

We designed and fabricated a hybrid PhC band-edge laser device and demonstrated its integration with other passive photonic components (waveguides and grating couplers) on a single  $\text{Si}_3\text{N}_4$  thin film platform. When optically excited, the CQD–PhC devices lased, emitting intense coherent light in the lateral directions predetermined by the particular band-edge mode employed, and were eventually out-coupled through grating couplers. Our scheme for the integration of active and passive photonic devices on a single chip guarantees a high coupling efficiency and thus should be an important milestone toward future high-density PICs with a variety of sophisticated functionalities.

# References

- [1] E. Yablonovitch, "Inhibited spontaneous emission in solid-state physics and electronics," *Physical Review Letters* **58**, 2059–2062 (1987).
- [2] S. Nojima, "Optical-gain enhancement in two-dimensional active photonic crystals," *Journal of Applied Physics* **90**, 545–551 (2001).
- [3] J. D. Joannopoulos, P. R. Villeneuve, and S. Fan, "Photonic crystals: Putting a new twist on light," *Nature* **386**, 143–149 (1997).
- [4] O. Painter, R. K. Lee, A. Scherer, A. Yariv, J. D. O'Brien, P. D. Dapkus, and I. Kim, "Two-dimensional photonic band-gap defect mode laser," *Science* **284**, 1819–1821 (1999).
- [5] D. Ohnishi, T. Okano, M. Imada, and S. Noda, "Room temperature continuous wave operation of a surface-emitting two-dimensional photonic crystal diode laser," *Optics Express* **12**, 1562–1568 (2004).
- [6] M. Nomura, S. Iwamoto, K. Watanabe, N. Kumagai, Y. Nakata, S. Ishida, and Y. Arakawa, "Room temperature continuous-wave lasing in photonic crystal nanocavity," *Optics Express* **14**, 6308–6315 (2006).
- [7] H.-G. Park, S.-H. Kim, S.-H. Kwon, Y.-G. Ju, J.-K. Yang, J.-H. Baek, S.-B. Kim, and Y.-H. Lee, "Electrically driven single-cell photonic crystal laser," *Science* **305**, 1444–1447 (2004).
- [8] H.-G. Park, C. J. Barrelet, Y. Wu, B. Tian, F. Qian, C. M. Lieber, "A wavelength-selective photonic-crystal waveguide coupled to a nanowire light source," *Nature Photonics* **2**, 622–626 (2008).

- [9] M. Tchernycheva, A. Messanvi, A. de Luna Bugallo, G. Jacopin, P. Lavenus, L. Rigutti, H. Zhang, Y. Halioua, F. H. Julien, J. Eymery, and C. Durand, "Integrated photonic platform based on InGaN/GaN nanowire emitters and detectors," *Nano Letters* **14**, 3515–3520 (2014).
- [10] L. Pavesi, and G. Guillot, *Optical interconnects: The silicon approach* (Springer, 2007)
- [11] J. P. Dowling, M. Scalora, M. J. Bloemer, and C. M. Bowden, "The photonic band edge laser: A new approach to gain enhancement," *Journal of Applied Physics* **75**, 1896–1899 (1994).
- [12] M. Imada, A. Chutinan, S. Noda, and M. Mochizuki, "Multidirectionally distributed feedback photonic crystal lasers," *Physical Review B* **65**, 195306 (2002).
- [13] R. M. Cazo, C. L. Barbosa, H. T. Hattori, V. M. Schneider, "Steady-state analysis of a directional square lattice band-edge photonic crystal lasers," *Microwave and Optical Technology Letters* **46**, 210–214 (2005).

# Chapter 3

## Continuously tunable colloidal quantum dot distributed feedback lasers integrated on chirped grating

### 3.1. Introduction

CQD-based lasers have been recently reported in a variety of type including vertical cavity surface emitting lasers (VCSELs) [1-3], whispering gallery mode (WGM) [4,5], PhC [6] and distributed feedback (DFB) types [7-10]. In addition to these high-Q cavity structures, improving the lasing performance is also studied in such a way as suppressing Auger recombination of CQD materials [11]. Here, I have implemented a CQD DFB laser with a single mode and a surface emitting characteristics capable of continuously selecting the emission wavelength. In general case of fabrication of DFB laser, formation of a corrugated structure is essential. For this purpose, e-beam lithography or laser interference lithography (LIL) is mainly used. The E-beam lithography method can draw various patterns in a direct writing manner, but costs highly and has low throughput. The LIL method is advantageous in that it can generate large-area sub-micron periodic patterns without masks at low cost and high throughput [12], but it is known that it is difficult to make aperiodic or various patterns.

To realize the tunable characteristics of DFB laser, a chirped grating structure whose period changes gradually according to changing of the position is introduced. Chirped gratings have been commonly used for compensating of dispersion characteristics in fiber [13-15] and de-multiplexing [16-19]. In fabricating these gratings, several kinds of methods have been mainly utilized such as E-beam lithography [20], tapering and stretching [21,22], and LIL method using refractive optical elements [23,24]. I fabricated a period-chirped grating through a LIL method using a concave mirror in a Lloyd mirror type setup [25]. Our method can be helpful to forming patterns with various periods at once while maintaining the merits of LIL. It is not only more effective than conventional direct patterning methods such as e-beam lithography and focused ion beam (FIB), but also has better alignment difficulty than LIL method using lenses. I completed the structure by wet-transferring a CQD film of a specific thickness onto a period-chirped grating formed on an optically transparent quartz substrate [26]. The formed DFB laser has progressively changing wavelengths as the pump position changes continuously under optical pump conditions. This method is effective for fabricating a large-area laser with various wavelengths as seen in this study. Further, it can be used as a light emitting device based on various gain materials, and it can be effectively used for passive device fabrication such as selective filters based on period variations.

## 3.2. Device design and calculation

### 3.2.1. Continuously tunable distributed feedback laser

The scheme of the proposed device is shown in Fig. 3-2-1. I fabricated a diffraction grating pattern in which the period gradually changed on the surface of a rigid and flat quartz ( $n = 1.46$ ) substrate. And a CQD ( $n = 1.77$ ) film of constant thickness emitting a red light was formed thereon. In this structure, the CQD layer forms an asymmetric waveguide with air and air-quartz grating substrates. The wave passing through this waveguide forms a DFB mode through modulation by the grating structure. I designed periods of the grating so that it has resonance at the 2nd order Bragg wavelength ( $\lambda = n_{\text{eff}}\Lambda$ ) and shows surface emitting characteristics.

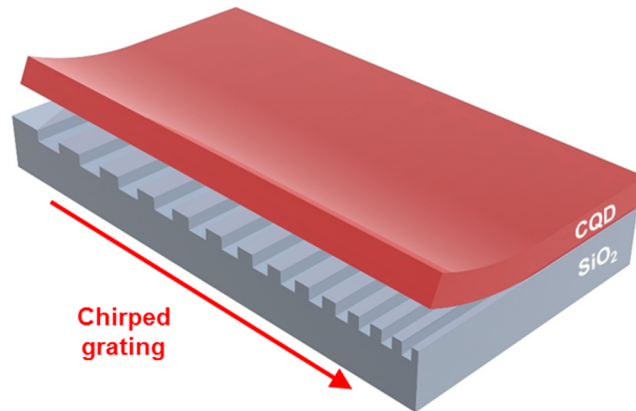


Figure 3-2-1 Schematic of continuously tunable CQD-DFB laser.

I set the thickness of the CQD layer for efficient laser oscillation, with the depth of the quartz grating fixed at 40 nm. As shown in Fig. 3-2-2, the CQD film thickness is well guided in the 1st order TE mode while suppressing the competitive TM mode in the guiding mode. The thickness of the CQD film is about 165 nm. Fig. 3-2-3 shows a part of the transverse electric photonic band structure of a DFB laser with a CQD film on a SiO<sub>2</sub> grating structure with a constant period by FDTD method. I chose modes at  $k_x = 0$  or the 2<sup>nd</sup> order band-edge modes for laser oscillation. In principle, two modes can exist on the band-edge with a wavelength difference of several nanometers, but one mode is lossy due to its symmetry and the other remains relatively longer in the CQD slab [27]. In addition, it can be confirmed that the quality factor ratio ( $Q_2^\perp/Q_1^\perp$ ) of the two modes has a value of approximately  $10^3$ . Among them, the electric field profile of the dominant mode can be seen as shown in Fig. 3-2-4. This time, it can be seen that the electric field distribution of the mode has a high energy overlap of about 76% with the gain material CQD layer.

Fig. 3-2-5 shows how the wavelength of the dominant DFB mode changes with the period of the quartz grating by FDTD method. The shade region is the theoretical mode wavelength variation range with a sample length of 1 cm. In each calculation, it is assumed that the grating period is locally constant, and the periodic structure is assumed to be infinite in the period. For our sample, I assume that the change is not large given the optical pump size ( $\sim 500 \mu\text{m}$ ), as the period changes about 12.5 nm for a 1 cm position change. The mode wavelength tends to monotonously increase as the grating period increases.

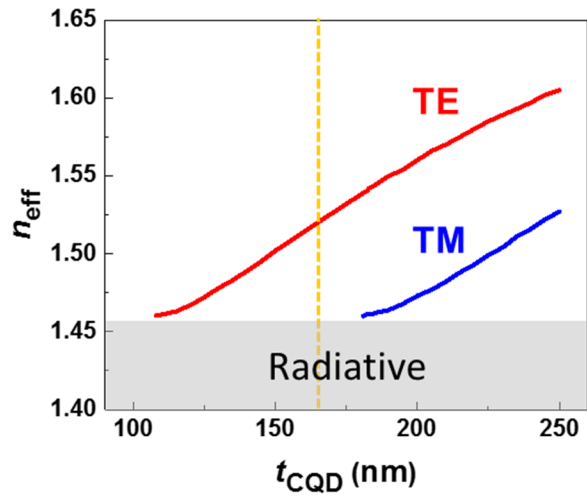


Figure 3-2-2 CQD film thickness dependence of effective index of fundamental guided modes. Yellow dashed line indicates film thickness of fabricated device.

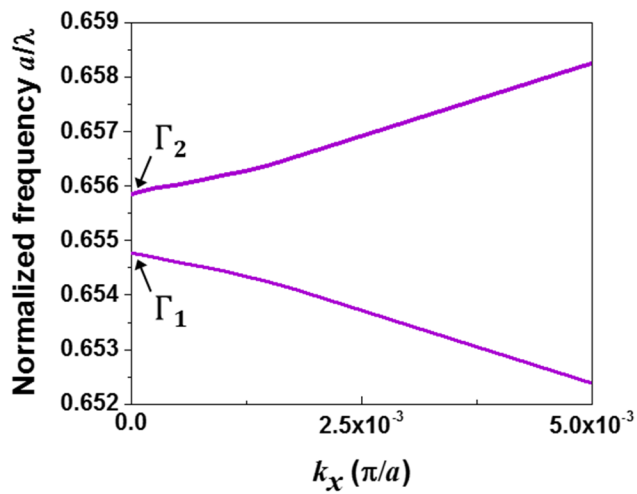


Figure 3-2-3 Dispersion relation of DFB laser near photonic band-edge.

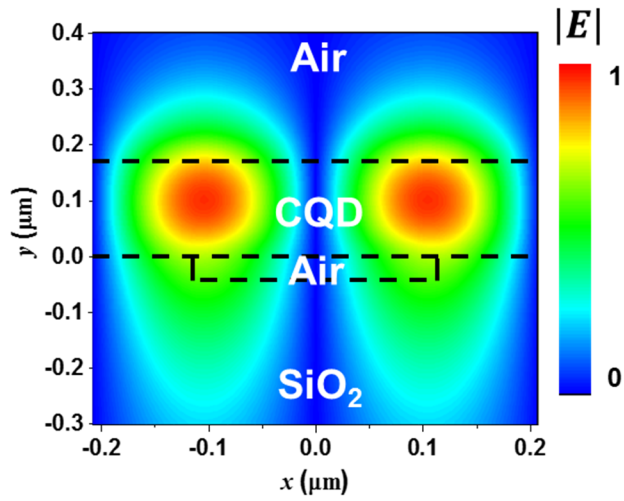


Figure 3-2-4 FDTD-simulated electric field profile of TE resonance mode.

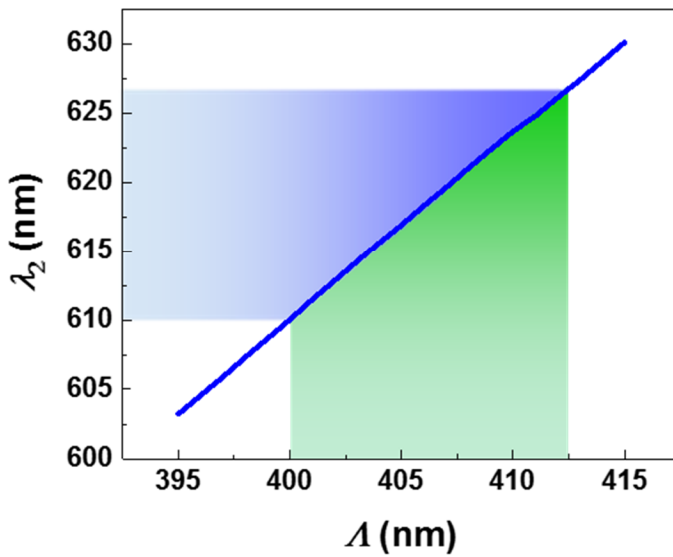


Figure 3-2-5 Tunability of DFB laser wavelength. Mode wavelengths are calculated by FDTD method.

### 3.3. Device fabrication

#### 3.3.1. Chirped grating generated by laser interference technique

To fabricate a grating with a gradually changing period, I used laser interference lithography with a modified Lloyd mirror setup. A diode laser with a wavelength of 405 nm passed through a spatial filter consisting of an objective lens and a pinhole to form an interference pattern of light incident directly on the sample and reflected on the mirror. As shown in Fig. 3-3-1, when the cylindrical mirror is used instead of the conventional flat mirror in the mirror stage, the angle of the incident beam is varied according to the position of the sample. As a result, the period of line grating formed on the surface is also varied. The period is expressed in the form of  $\Lambda = \lambda / (\sin \theta_1 + \sin \theta_2)$  ( $\lambda$  is wavelength of laser,  $\theta_1$  is the incident angle of light entering the sample directly,  $\theta_2$  is the angle of incidence on the sample surface reflected by the mirror). The nominal period of the sample can be adjusted, and the range of the period is determined on the sample according to the geometry of the setup including the mirror used. By using the notation in Fig. 3-3-2, following equation are derived,

$$\Lambda(\varphi) = \frac{\lambda}{\sin \theta_1 + \sin \theta_2} = \frac{\lambda}{\sin \theta_1 + \sin (\theta_1 - 2\varphi)}, \quad \rho = R \sin \varphi,$$

$$\delta_0 = \rho_0 \tan \theta_1, \quad \tan(\theta_1 - 2\varphi) = \frac{\delta + \delta_0 - R + \sqrt{R^2 - \rho^2}}{\rho + \rho_0},$$

$$\delta(\varphi) = (R \sin \varphi + \rho_0) \tan(\theta_1 - 2\varphi) - \rho_0 \tan \theta_1 + R(1 - \cos \varphi).$$

These equations are combined and the relationship between the grating period and the position  $\delta$  can be obtained. A cylindrical mirror (surface  $\lambda/4$  at 633 nm) with a curvature radius of 1150 mm and a size of 8 cm by 8 cm is used to form a diffraction grating. This mirror is dielectric coated and is designed to have high

reflectivity ( $> 0.99$ ) at 405 nm laser wavelength. In Figure 3-3-3, in this setup configuration, the grating period according to the position  $\delta$  ( $\theta_1 = \theta_2$ ,  $\delta = 0$ ) on the stage is calculated by the geometric method when the reference incidence angle  $\theta_1$  is  $30.4^\circ$ . Due to the geometrical nature of cylindrical mirror, the greater the value of the reference period, the larger the periodic variation. In actual sample fabrication, the resonance mode of the laser structure is in the emission wavelength range of the CQD material using the incident angle condition of  $30.4^\circ$  with a reference period of 400 nm. The position of the sample was set so that a resist pattern having a period range of about 400 to 412.5 nm could be formed on the surface through a LIL using a cylindrical mirror on a square of 1 cm by 1 cm square fused quartz substrate, and the resist pattern was transferred into substrate using RIE process.

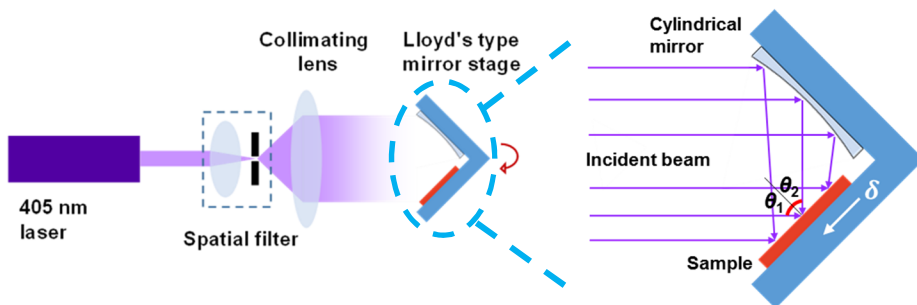


Figure 3-3-1 Modified Lloyd's mirror stage by using cylindrical mirror. Laser incident angles to sample plane is marked as  $\theta_1$ ,  $\theta_2$ .

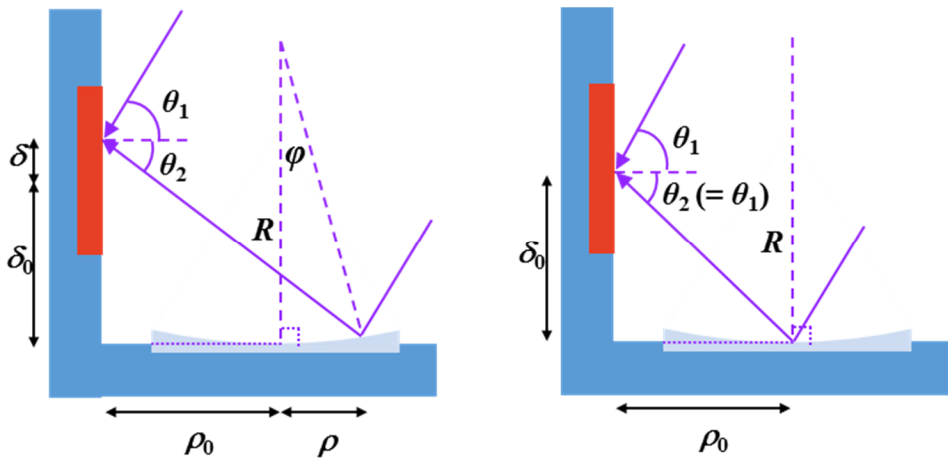


Figure 3-3-2 Detailed picture of cylindrical mirror stage

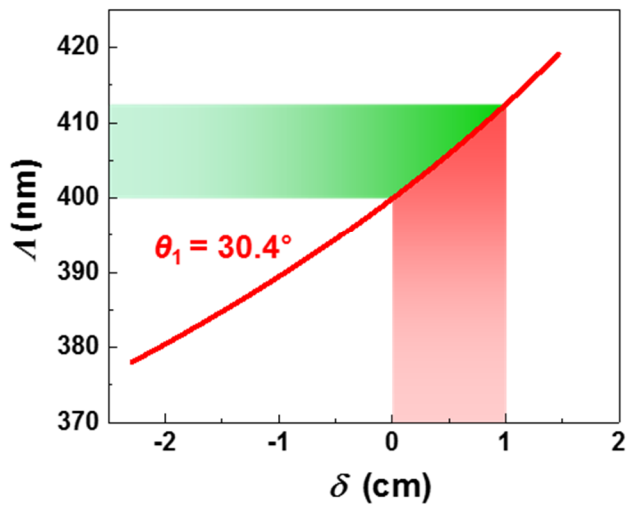


Figure 3-3-3 Calculation of tunability of period of chirped grating. For an incident angle ( $\theta_1 = 30.4^\circ$ ), grating period ranges are plotted.

### 3.3.2. Wet transfer of colloidal quantum dots film

In addition, a red light emitting CQD material as an optical gain material was prepared. The CdSe/CdS/ZnS CQD material of the core/shell/shell structure I used is chemically synthesized and has a center emission wavelength of about 615 nm and an emission wavelength width of 30 nm. A CQD film having a constant thickness was formed through a wet-transfer method on the period-varying quartz grating. The wet-transfer method uses a polymerized handling layer (PMMA) and a sacrificial layer (PVA) to transfer the CQD layer onto the grating via water. A dense CQD layer of uniform thickness with low scattering can be uniformly formed as shown in Fig. 3-3-4.

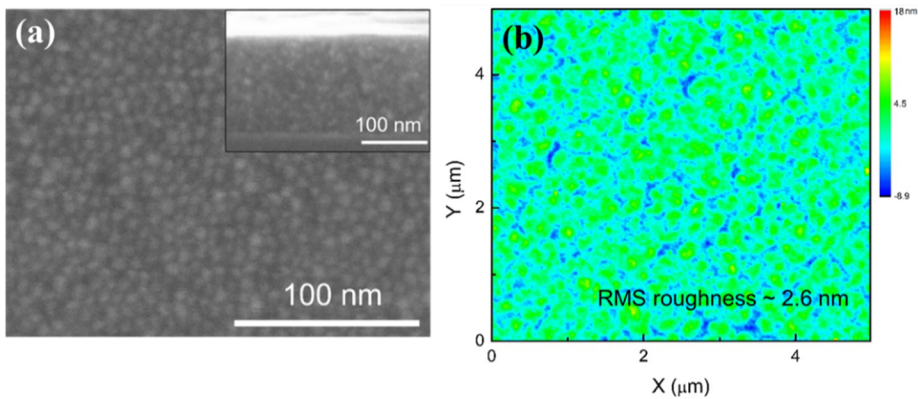


Figure 3-3-4 (a) SEM image of wet-transferred CQD film. (b) AFM image of a wet-transferred CQD film

### 3.3.3. Continuously tunable laser device

Fig. 3-3-5 is images of a DFB laser sample I have actually fabricated. It can be seen from Fig. 3-3-5 (a) that the CQD film is relatively uniformly formed on the transparent substrate, and it can be confirmed that the overall area of sample is shining by diffraction as in the case where the white light source is incident at a specific angle. In addition, Fig. 3-3-5 (b) shows an SEM image of the sample cross section, showing that a CQD layer with a constant thickness floats on the quartz grating. The structure thus formed enhances vertical confinement by including a low index of air-void and can improve the index contrast of two materials arranged periodically.

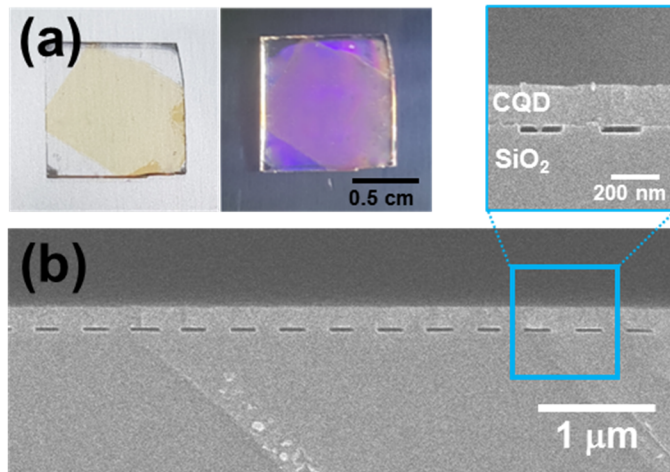


Figure 3-3-5 (a) Photograph images of the sample. (b) SEM image of fabricated DFB laser. Upper right image shows magnified layered structure.

## 3.4. Optical measurements and analyses

### 3.4.1. Distributed feedback laser characteristics

This section shows the laser characteristics of the fabricated samples. Fig. 3-4-1 shows spectra at several excitation energy when Nd: YAG laser (400 ps pulse width and 1 kHz repetition rate) with a wavelength of 532 nm is pumped to an area of width of 500  $\mu\text{m}$  at one position ( $x = 200 \mu\text{m}$ ,  $x$  is the center position of 1  $\text{cm}^2$  sample) of the laser sample. The micro-PL measurements set-up utilized in chapter 2 was modified by using cylindrical lens (effective focal length  $f = 25.0 \text{ mm}$ ;  $\text{NA} = 0.50$ ) and a slit to pump sufficient power into the DFB laser. Fig. 3-4-2 shows the light in - light out curve and the linewidth according to the pump density, which allows the laser threshold characteristics to be clearly seen. Fig. 3-4-3 shows the polarization characteristics of the laser emission. It can be seen that the measured laser mainly has the electric field direction component parallel to the grating line, and it has the TE mode characteristic as designed.

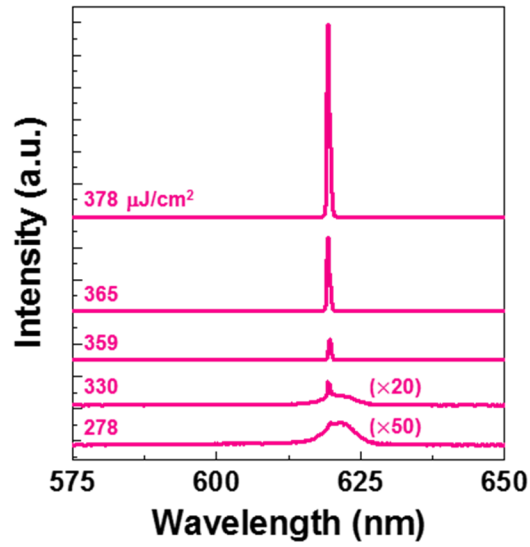


Figure 3-4-1 Photoluminescence spectra at various excitation pulse energies.

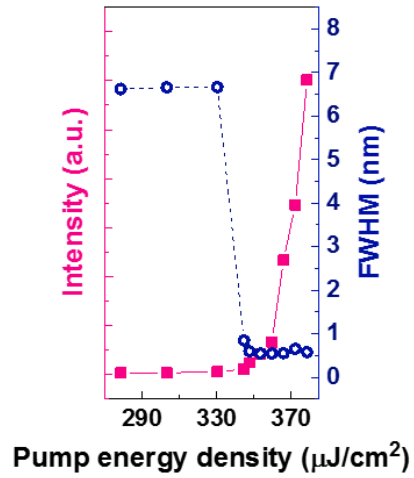


Figure 3-4-2 Light-in vs. light-out. (magenta), linewidth depending on pump energy (dark blue)

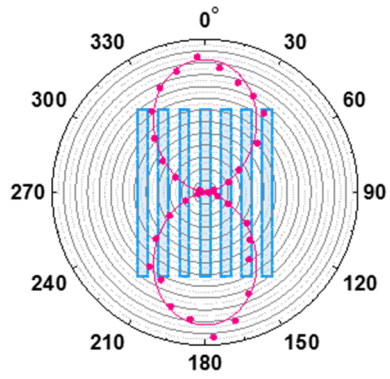


Figure 3-4-3 Polarization distribution. Grating lines are parallel to  $0^\circ$ ,  $180^\circ$  directions.

### 3.4.2. Position dependence of the laser

Fig. 3-4-4 shows the laser wavelength recorded at 200  $\mu\text{m}$  intervals on the sample. Each of the lasers had a single mode characteristic, and it was confirmed that the mode wavelength was monotonically increased by moving the measurement position from -2.8 mm to 2.8 mm. Within a 5.6 mm section of the sample, the wavelength change is 9.79 nm, which has a slope of 1.75 nm/mm. Also, the dark blue dotted line is obtained from the geometric calculation and the FDTD simulation from the cylindrical mirror specification, which I used. The wavelength change of 9.46 nm is expected for 5.6 mm section and has a slope value of 1.69 nm/mm. Figure 3-4-5 (a) shows the spectra of the lasers measured at 10 locations with different periods on the sample. Each position was selected to be 600  $\mu\text{m}$  away from the direction of the period as shown in Fig. 3-4-4, and the laser phenomenon with various wavelengths was confirmed. Figure 3-4-4 (b) shows the measurement of the lasing threshold at each position, which shows a relatively constant value with an average value of 404  $\mu\text{J}/\text{cm}^2$  and a standard deviation of 28  $\mu\text{J}/\text{cm}^2$ , although there is a difference depending on the position. This means that the sample is fabricated with even quality over sample positions.

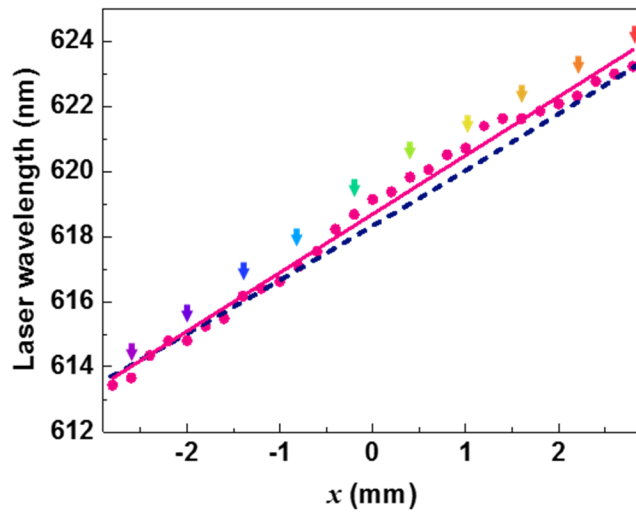


Figure 3-4-4 Position dependence of lasing wavelength. Experimental data are shown as magenta color and calculation data are plotted as dark blue for comparison.

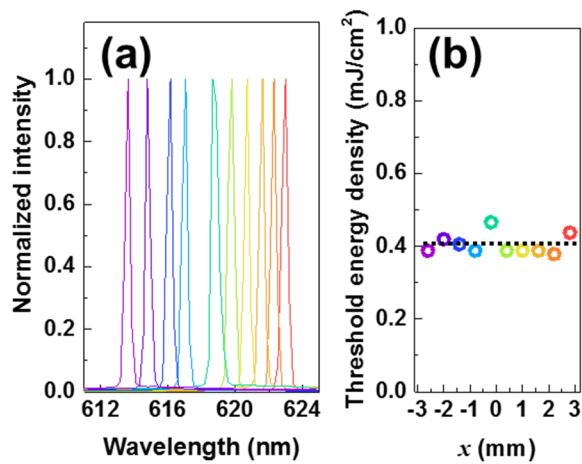


Figure 3-4-5 (a) Selected laser spectra taken at equal interval of 600  $\mu\text{m}$ . (b) Threshold density variation over sample position.

### 3.5. Summary

In this study, I fabricated CQDs DFB laser integrated on a chirped grating, of which lasing wavelength changes continuously as a function of location. A period-chirped surface grating is fabricated using a modified Lloyd-type LIL setup where a flat mirror is replaced with a concave one. A dense red-emitting CdSe/CdS/ZnS CQDs film is spin-casted on silicon substrate, which is subsequently released and transferred onto a period-chirped surface grating formed on a quartz plate. Upon optical excitation, the fabricated DFB laser structure exhibits a single-mode lasing action at laser threshold of  $\sim 400 \mu\text{J}/\text{cm}^2$ . The lasing wavelength is observed to shift gradually from 613.4 nm to 623.2 nm as the pump spots is scanned over a distance of  $\sim 5.6$  mm. These results demonstrate that the modified LIL setup can produce high quality chirped gratings at low cost, which should be useful for various sophisticated photonic devices.

# References

- [1] C. Dang, J. Lee, C. Breen, J. S. Steckel, S. Coe-Sullivan, A. Nurmikko, “Red, green and blue lasing enabled by single-exciton gain in colloidal quantum dot films,” *Nature Nanotechnology* **7**, 335-339 (2012).
- [2] B. Guzelturk, Y. Kelestemur, K. Gungor, A. Yeltik, M. Z. Akgul, Y. Wang, R. Chen, C. Dang, H. Sun, H. V. Demir, “Stable and low-threshold optical gain in CdSe/CdS quantum dots: an all-colloidal frequency up-converted laser,” *Advanced Materials* **27**, 2741-2746 (2015).
- [3] H. Kim, K.-S. Cho, H. Jeong, J. Kim, C.-W. Lee, W.-K. Koh, Y.-G. Roh, S. W. Hwang, Y. Park, “Single-mode lasing from a monolithic microcavity with few-monolayer-thick quantum dot films,” *ACS Photonics* **3**, 1536-1541 (2016).
- [4] C. H. Lin, Q. Zeng, E. Lafalce, M. J. Smith, S. T. Malak, J. Jung, Y. Yoon, Z. Lin, Z. V. Vardeny, V. V. Tsukruk, “Large-scale robust quantum dot microdisk lasers with controlled high quality cavity modes,” *Advanced Optical Materials*, **5**, 1700011 (2017).
- [5] W. Xie, T. Stöferle, G. Rainò, T. Aubert, S. Bisschop, Y. Zhu, R. F. Mahrt, P. Geiregat, E. Brainis, Z. Hens, D. Van Thourhout, “On-chip integrated quantum-dot–silicon-nitride microdisk lasers,” *Advanced Materials* **29**, 1604866 (2017).
- [6] H. Chang, K. Min, M. Lee, M. Kang, Y. Park, K.-S. Cho, Y.-G. Roh, S. W. Hwang, H. Jeon, “Colloidal quantum dot lasers built on a passive two-dimensional photonic crystal backbone,” *Nanoscale* **8**, 6571-6576 (2016).

- [7] C. Dang, J. Lee, K. Roh, H. Kim, S. Ahn, H. Jeon, C. Breen, J. S. Steckel, S. Coe-Sullivan, A. Nurmikko, “Highly efficient, spatially coherent distributed feedback lasers from dense colloidal quantum dot films” *Applied Physics Letters* **103**, 171104 (2013).
- [8] C. Foucher, B. Guilhabert, N. Laurand, M. D. Dawson, “Wavelength-tunable colloidal quantum dot laser on ultra-thin flexible glass,” *Applied Physics Letters* **104**, 141108 (2014).
- [9] Y. Zhu, W. Xie, S. Bisschop, T. Aubert, E. Brainis, P. Geiregat, Z. Hens, D. Van Thourhout, “On-chip single-mode distributed feedback colloidal quantum dot laser under nanosecond pumping,” *ACS Photonics* **4**, 2446-2452 (2017).
- [10] F. Prins, D. K. Kim, J. Cui, E. De Leo, L. L. Spiegel, K. M. McPeak, D. J. Norris, “Direct patterning of colloidal quantum-dot thin films for enhanced and spectrally selective out-coupling of emission,” *Nano letters* **17**, 1319-1325 (2017).
- [11] F. Fan, O. Voznyy, R. P. Sabatini, K.T. Bicanic, M. M. Adachi, J. R. McBride, K. R. Reid, Y.-S. Park, X. Li, A. Jain, R. Quintero-Bermudez, M. Saravanapavanantham, M. Liu, M. Korkusinski, P. Hawrylak, V. I. Klimov, S. J. Rosenthal, S. Hoogland, E. H. Sargent, “Continuous-wave lasing in colloidal quantum dot solids enabled by facet-selective epitaxy,” *Nature* **544**, 75-79 (2017).
- [12] H. van Wolferen, L. Abelmann, *Lithography: Principles, Processes and Materials*, (Nova Science 2011).
- [13] F. Ouellette, “Dispersion cancellation using linearly chirped Bragg grating filters in optical waveguides,” *Optics letters*, **12**, 847-849 (1987).
- [14] K. O. Hill, F. Bilodeau, B. Malo, T. Kitagawa, S. Theriault, D. C. Johnson, J. Albert, K. Takiguchi, “Chirped in-fiber Bragg gratings for compensation of optical-fiber dispersion,” *Optics letters* **19**, 1314-1316 (1994).

- [15] S. Lee, R. Khosravani, J. Peng, V. Grubsky, D. S. Starodubov, A. E. Willner, J. Feinberg, "Adjustable compensation of polarization mode dispersion using a high-birefringence nonlinearly chirped fiber Bragg grating," *IEEE Photonics technology letters* **11**, 1277-1279 (1999).
- [16] A. C. Livanos, A. Katzir, A. Yariv, C. S. Hong, "Chirped-grating demultiplexers in dielectric waveguides," *Applied Physics Letters* **30**, 519-521 (1977).
- [17] M. G. Xu, A. T. Alavie, R. Maaskant, M. M. Ohn, "Tunable fibre bandpass filter based on a linearly chirped fibre Bragg grating for wavelength demultiplexing," *Electronics Letters* **32**, 1918-1919 (1996).
- [18] Y. J. Lin, S.-L. Lee, "InP-based 1.3/1.55  $\mu\text{m}$  wavelength demultiplexer with multimode interference and chirped grating," *Optical and Quantum Electronics* **34**, 1201-1212 (2002).
- [19] R. Romero, O. Frazão, F. Floreani, L. Zhang, P. V. S. Marques, H. M. Salgado, "Chirped fibre Bragg grating based multiplexer and demultiplexer for DWDM applications," *Optics and Lasers in Engineering* **43**, 987-994 (2005).
- [20] R. Steingrüber, M. Möhrle, A. Sigmund, W. Fürst, "Continuously chirped gratings for DFB-lasers fabricated by direct write electron-beam lithography," *Microelectronic engineering* **61**, 331-335 (2002).
- [21] M. A. Putnam, G. M. Williams, E. J. Friebele, "Fabrication of tapered, strain-gradient chirped fibre Bragg gratings," *Electronics Letters* **31**, 309-310 (1995).
- [22] V. Lien, Y. Wu, D. Zhang, Y. Berdichevsky, J. Choi, Y. H. Lo, "A novel technology for fabricating gratings of any chirp characteristics by design," *IEEE Photonics Technology Letters* **15**, 712-714 (2003).
- [23] D. A. Bryan, J. K. Powers, "Improved holography for chirped gratings," *Optics letters* **5**, 407-409 (1980).

- [24] K. Liu, H. Xu, H. Hu, Q. Gan, A. N. Cartwright, "One-Step fabrication of graded rainbow-colored holographic photopolymer reflection gratings," *Advanced Materials* **24**, 1604-1609 (2012).
- [25] H. Kim, H. Jung, D. H. Lee, K. B. Lee, H. Jeon, "Period-chirped gratings fabricated by laser interference lithography with a concave Lloyd's mirror," *Applied optics* **55**, 354-359 (2016).
- [26] C. Han, H. Jung, J. Lee, M. Lee, Y. Park, K.-S. Cho, H. Jeon, "Wet-transfer of freestanding dense colloidal quantum dot films and their photonic device application," *Advanced Materials Technologies* **3**, 1700291 (2018).
- [27] R. Kazarinov, C. Henry, "Second-order distributed feedback lasers with mode selection provided by first-order radiation losses," *IEEE Journal of Quantum Electronics* **21**, 144-150 (1985).



# Appendix

## Distributed feedback laser with physically transient characteristics using bio-compatible fluorescein-doped silk solution

### A.1. Introduction

The growing demand for bio-optical devices in healthcare has stimulated interest in the use of biomaterials due to their bio- and eco-friendly properties [1,2]. Silk fibroin, the natural protein extracted from the *Bombyx mori* caterpillar, is gaining an increasingly prominent role as an optical biomaterial [3]. The self-assembled silk film shows optical transparency and easy nano-structuring at optical wavelengths. In addition, biologically or optically active dopants such as enzymes, drugs, and dyes can be incorporated into the silk fibroin matrix under all water-based and mild processes, thereby enabling a functionalized nano-optical device to be generated [3,4]. To date, silk fibroin has been applied as a bio-functionalized resist for lithography [5,6], a bio-ink for inkjet printing [7], and a nonlinear optical material [8]. Various silk-based optical devices have been realized, including PhCs [9-11], organic DFB lasers [12-14], metal-insulator-metal resonators [15,16], and metamaterials [17,18]. Moreover, the biodegradability, renewability, and low cost of silk fibroin would enable a physically transient and water-disposable optical device [19], as an optical

version of the recently reported transient electronic device [20,21].

Silk-based and other biomaterial-based optics are strongly linked to the optics of organic materials. Organics are ideally suited for applications that require color tunability, a large active area, mechanical flexibility, and low-cost processing in optics [22]. In particular, as a light source, organic lasers are easy to fabricate and do not require elaborate processing, while they emit highly coherent light and show broad tuning ranges. With reports of their use for explosives detection, on-chip spectroscopy, and data communications, organic lasers cover a broad scope of applications [23-26]. However, a short lifetime, pulse operation, and optical pumping are inherent and insurmountable limitations of organic lasers for many applications [22]. Therefore, the use of organic lasers as a disposable and transient light source is more appealing with the advantage of low-cost, especially for various spectroscopic applications in life or environmental science.

Here, I report the use of optically activated silk bio-ink for the realization of a physically transient DFB laser, utilizing a simple and entirely green spin-coating process on a large area 1D fused silica grating. Sodium fluorescein, a dye used for diagnostics in ophthalmology and optometry, was used to activate silk bio-ink optically [27]. The resulting DFB structure showed single mode lasing at the wavelength of 555 nm and had a threshold of 13.6 mJ/cm<sup>2</sup>. The obtained laser structure had limited lifetime due to the degradability of organic silk active layer, but I was able to remove the used and degraded silk active layer by dipping in water for a few seconds and the washed fused silica grating could then become a new DFB laser by spin-coating the silk bio-ink. The threshold and the differential external quantum efficiency remained steady under the repetitive washing and re-coating process. In addition, the chemosensing capability of the physically transient silk DFB

laser was investigated using hydrochloride vapor as a model analyte.

## A.2. Device design and fabrication

### A.2.1. Physically transient distributed feedback laser using silk-bio ink

The scheme for using silk bio-ink to achieve a physically transient DFB laser is presented in Figure A-2-1. To obtain optically activated silk bio-ink, I prepared a blended aqueous solution by dissolving sodium fluorescein powder in a 6% aqueous silk solution to achieve a solidified silk film of 1% concentration of sodium fluorescein. A reusable fused silica substrate with a 1D surface grating was fabricated via a laser-interference-lithography (LIL) method, an inexpensive and reliable fabrication method for sophisticated structures across large areas [28,29]. The silk bio-ink was then spin-coated on the large area fused silica grating to yield a flat waveguide layer. Optical pumping induced the structure to emit single-mode laser radiation. After use, the silk layer was washed out and the fused silica grating was then ready to use again.

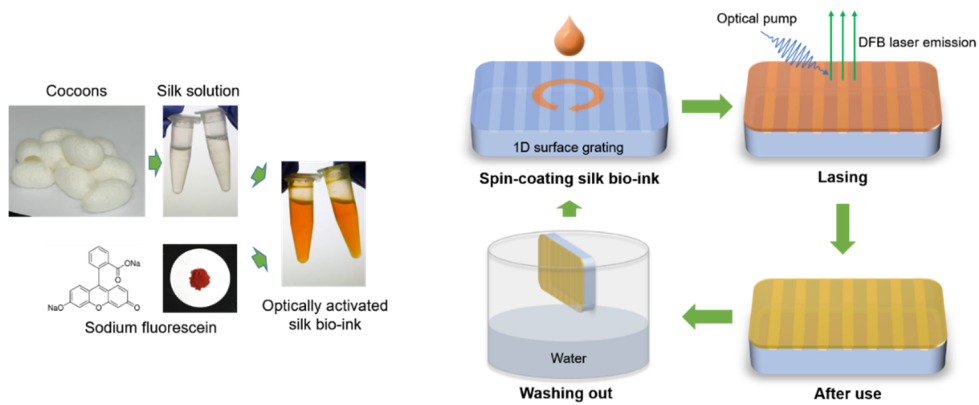


Figure A-2-1 Schematic configurations to show the working principle of the physically transient DFB laser using optically activated silk bio-ink and a permanently usable fused silica grating.

### A.2.2. Preparing silk bio-ink

For the preparing the silk aqueous solutions, cocoons of *Bombyx mori* caterpillars were boiled for 60 min in a solution of  $\text{Na}_2\text{CO}_3$  (0.02 M) to remove the sericin protein. The extracted fibroin was rinsed with distilled water and then dried in air for 24 h. After drying, the fibroin was dissolved in a LiBr solution (9.3 M) at 60 °C for 4 h, yielding a 20 wt% aqueous solution. The silk/LiBr solution was dialyzed against distilled water using a dialysis cassette (Slide-a-Lyzwe, Pierce, MWCO 3.5 K) at room temperature for two days until the solution reached a concentration of 6%. The obtained solution was purified using a centrifuge and a syringe filter with a pore size of 0.45- $\mu\text{m}$ . And optically activated solution was produced in a way where a silk aqueous solution of 6% concentration was mixed with sodium fluorescein salt to achieve silk of 99 wt% and sodium fluorescein of 1 wt%. In general, I can easily detect the lasing signal as the concentration of dye molecules is increased. However, over a certain concentration, the lasing performance worsens since the distance between the dye molecules becomes too close to take an independent role. The concentration of 1% is close to the maximum concentration I can obtain.

### A.2.3. Fluorescein doped-silk distributed feedback laser

Fig. A-2-2 (a) shows a photograph and the scanning electron microscopy (SEM) image of the fabricated fused silica grating with a 60 nm height, 370 nm pitch size ( $\Lambda$ ), and 60% duty cycle. The  $\Lambda$  was chosen to fall the wavelength ( $\lambda_{\text{Bragg}}$ ) of the second order DFB mode, determined by  $\lambda_{\text{Bragg}} = \Lambda n_{\text{eff}}$  ( $n_{\text{eff}}$ : the effective refractive index of the waveguide mode), within the photoluminescence (PL) of the sodium fluorescein dye (Fig. A-2-2 (b)). The cross-sectional SEM image and the atomic force microscopy (AFM) image in Fig. A-2-2 (c) and (d), respectively, reveal that the spin-coated silk waveguide layer has a very flat silk-air interface. Using the obtained physical parameters of the structure, I performed numerical simulations to investigate the optical modes. The FDTD method was used for simulations and the simulated spectrum is shown in Fig. A-2-3 (a). I could observe two modes at wavelengths of 551.8 and 554.9 nm, distinguished by polarization. In addition, these two modes induced the DFB lasing, which will be shown in a later section. The main peak at 554.9 nm originates from the TE waveguide mode (Fig. A-2-3 (b)), while the satellite peak at 551.8 nm refers to the TM waveguide mode [30].

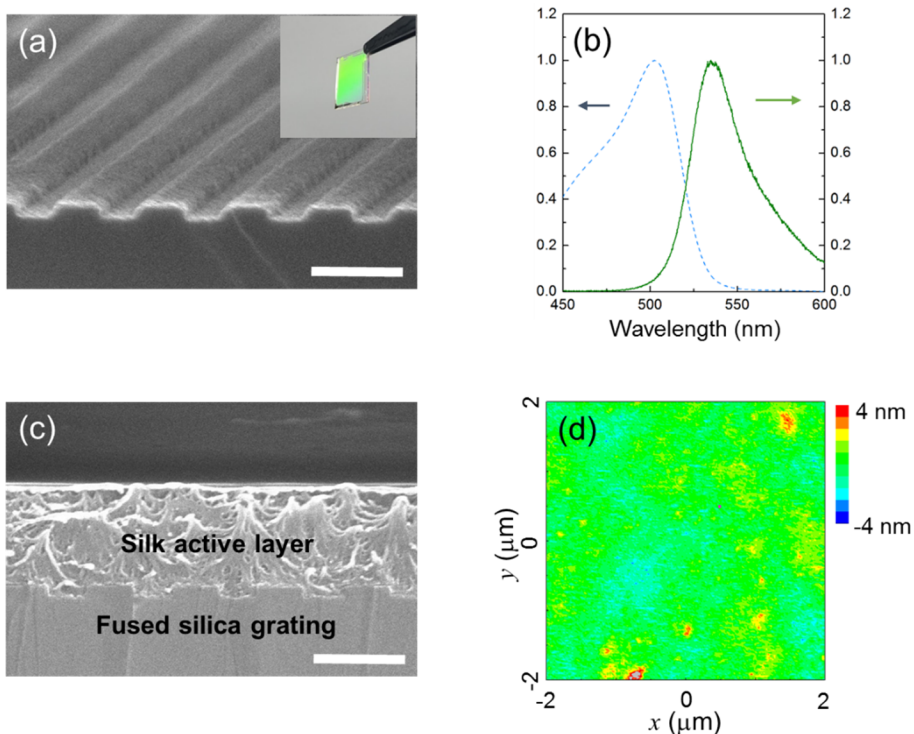


Figure A-2-2 (a) Scanning electron microscopy (SEM) image of the fused silica grating generated by the laser-interference-lithography (LIL) method. Inset shows a photograph of the grating, showing green diffraction over the entire surface. (b) Absorption (dashed curve) and photoluminescence (solid curve) spectra for a thin film of sodium fluorescein doped silk. (c) Cross-sectional SEM image of the silk bio-ink coated fused silica grating. (d) Atomic force microscopy (AFM) topographic image of the sample in (c). Scale bars in (b) and (c) indicate 350 nm.

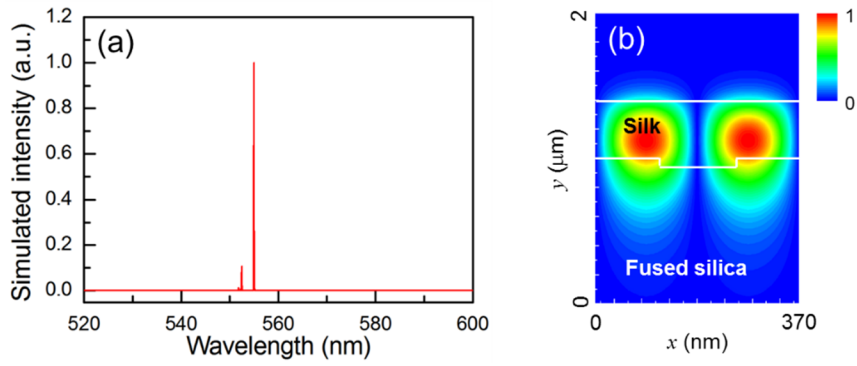


Figure A-2-3 (a) Simulated spectrum of the DFB structure. (b) Normalized electric field (parallel to the grating surface) intensity corresponding to the resonance mode at  $\lambda = 554.9$  nm.

## A.3. Optical measurements and analyses

### A.3.1. Optical characteristics of the physically transient distributed feedback laser

The optical characteristics of the fabricated DFB laser upon pulsed optical pumping were investigated. I used ns-laser pulses from a frequency tripled Nd:YAG laser ( $\lambda = 355$  nm) with a  $0.4 \times 3$  mm beam spot size. Fig. A-2-4 (a) exhibits a light-in versus light-out curve (LL curve), measuring the output energy as a function of input pumping energy. Narrow emission peaks ( $\Delta\lambda_{\text{FWHM}} \sim 0.46$  nm, twice the resolution limit of the spectrometer) at wavelengths of 551.8 nm and 555 nm (Fig. A-2-4 (b)) appeared for the pumping energy higher than around  $13.6$  mJ/cm<sup>2</sup>, of which the energy increased linearly as the pumping energy increased. The peak positions and mode spacing of the experimental results were in good agreement with the simulated spectrum. If necessary, the weak TM mode would be filtered out using a polarizer. The threshold energy was rather high when compared with the thresholds of the other reported organic DFB lasers [30,31], but the number would be reduced when the wavelength of the pumping source could be tuned to the absorption peak. Also, inducing high thermal conductive layer or higher index contrast structures, or other sophisticated structures [32] could give a better result in performance. Additionally, I investigated the lasing performance of the biological DFB laser while decreasing the concentration of the sodium fluorescein dye, since the dye molecules can interact with their neighbors at high concentrations and consequently show a lower quantum yield. The sodium fluorescein concentration used was close to the maximum value obtainable by dissolving as much of the dye as possible in water. As shown in Fig. A-2-5, the diluted active layer resulted in an increase of the threshold

energy, along with a decrease of the output energy.

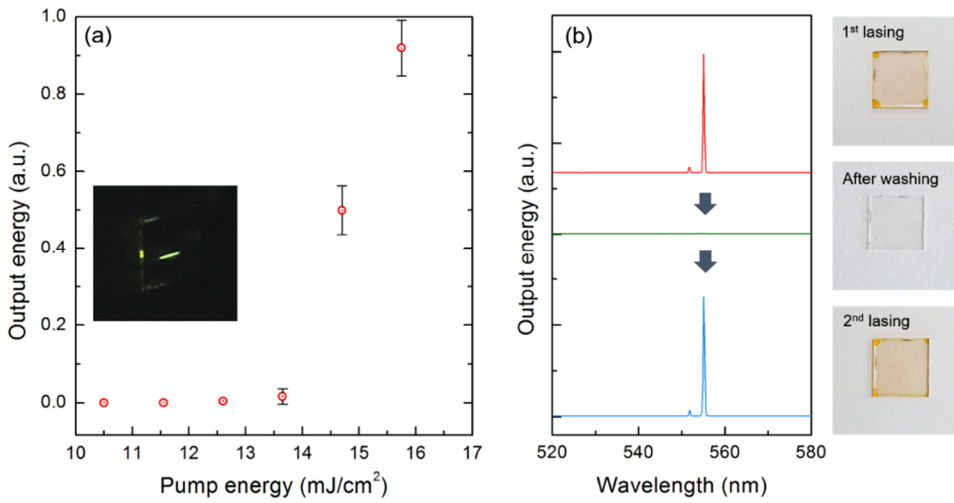


Figure A-2-4 (a) Optical characteristics of the physically transient DFB laser. (a) Output energies of the lasing peak as a function of the pump influence. The error bars represent the standard deviation calculated from 5 washing and re-coating trials. Inset shows a photographic image of the silk DFB laser under excitation. (b) Lasing spectra from the DFB laser. The lasing peak disappeared after washing out and reappeared after spin-coating the silk bio-ink.

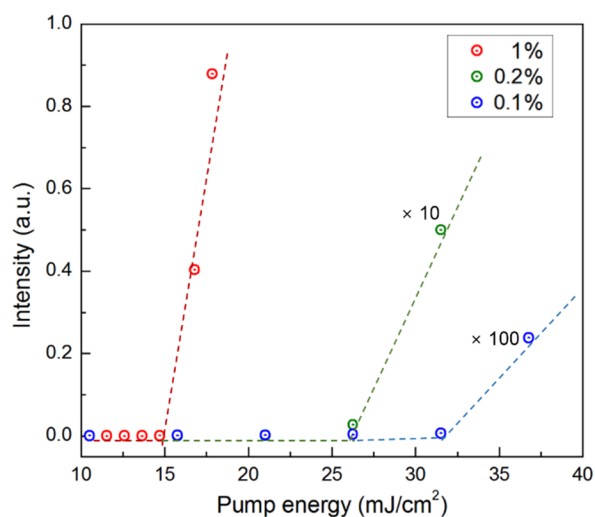


Figure A-2-5 Dependence of the DFB laser on sodium fluorescein concentration. Light-in versus light-out curves for three different concentrations: 0.1% (blue), 0.2% (green), and 1% (red).

As can be seen in Fig. A-2-6, the output power of obtained DFB laser decreased to the half after operating about 15s. The lifetime of the laser was too short to acquire consistent results for applications that require long-term exposure [22]. An important property to be confirmed here is the consistency of the LL curve and the peak positions after washing and re-coating since I am seeking new potential for the disposability and reusability of the biological DFB laser. The error bars of the output energy (Fig. A-2-4 (a)) are calculated as the standard deviation of the 5 washing and re-coating trials. When energy fluctuation of our Nd:YAG pumping laser and the integration time (0.5 s, corresponding to 5 pulse shots) of the spectrometer are considered, our result shows reliability and consistency, along with exactly the same lasing wavelength for all trials. Additionally, it is worth noting that the silk bio-ink is

cost-effective. The fused silica grating can be used permanently and could be a DFB laser by spin-coating the silk bio-ink at a cost of under USD ten cents. These results demonstrate that I can produce a stable and physically transient laser-emitting component using natural and biomedical materials at low cost, appealing to biomedical or environmental applications.

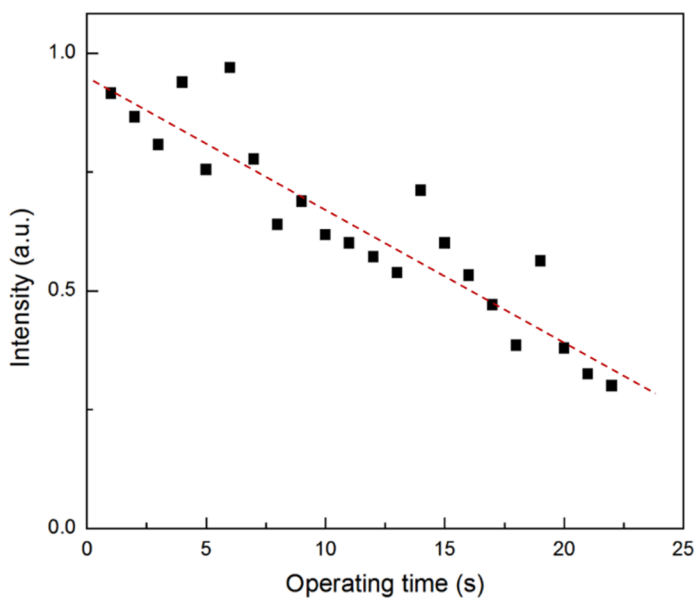


Figure A-2-6 Measured output energy as a function of the operating time.

### A.3.2. Application as a chemosensor to detect hydrogen chloride vapor

A possible application of the physically transient and silk based DFB lasers is their use as a fluorescent chemosensor to detect noxious vapors. In this study, hydrochloric (HCl) acid fume, which is widely used but highly toxic, was chosen as an analyte. The HCl vapor diffusing into the silk matrix interacted with the immobilized sodium fluorescein molecules and consequently diminished its optical activity [33]. Fig. A-2-7 (a) shows photographs and emission spectra before/after exposing the silk DFB laser to the HCl fume for 1 min. To exclude the effect of degradation from operating time, I optically pumped the newly fabricated laser sample once before HCl vapor exposure. After that, I washed out the sample by dipping in water and re-coated the sodium fluorescein doped silk solution. The re-coated sample was exposed to HCl vapor and was operated under optical pumping. The optical activity of the silk DFB laser, which showed a sharp and strong lasing peak even at the low pump energy of  $14.7 \text{ mJ/cm}^2$ , disappeared and a very weak emission was displayed at the high pump energy of  $63 \text{ mJ/cm}^2$  after the HCl vapor exposure, while the scorched silk layer formed a yellowish color. A simple washing and re-coating process could turn the scorched silk DFB laser into a new laser. To better understand the origins of the quenching, I investigated the optical characteristics of absorption and fluorescence for the sodium fluorescein doped silk film before/after the HCl vapor exposure (Fig. A-2-7 (b)). Interestingly, the absorption peak was blue-shifted after the exposure, while the fluorescence peak was decreased at the same wavelength. Fluorescein and its variations have strong pH dependence in fluorescence and absorption due to the occurrence of protolytic reactions in the excited state [34,35]. Strong acids can induce cation species that reduce the quantum yield and the blue-shift of absorption. Additionally, optical

transmissions of a pure silk film over a broad spectral range were measured before/after exposing the sample to the HCl vapor to investigate the effect of the HCl vapor on the silk matrix (Fig. A-2-8). I could observe that optical transparency was preserved well under the acid vapor exposure, indicating that the silk fibroin could be a reliable and chemically stable matrix material for sensing the applications of organic DFB lasers. It would be possible to enlarge the scope of applications such as reusable food sensors detecting amine gas by utilizing the material traits of sodium fluorescein.

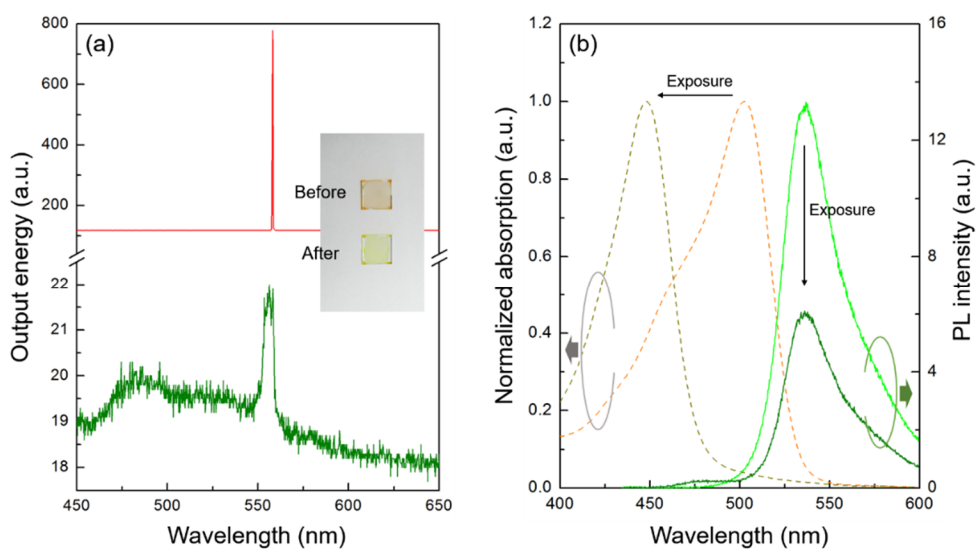


Figure A-2-7 Application as a chemosensor to detect HCl vapor. (a) Lasing spectra showing the responses before (red) and after (green) exposure to HCl vapor. Inset shows a photograph image of the silk DFB laser. (b) Absorption (dashed curves) and PL (solid curves) spectra before and after 1 minute exposure to HCl vapor.

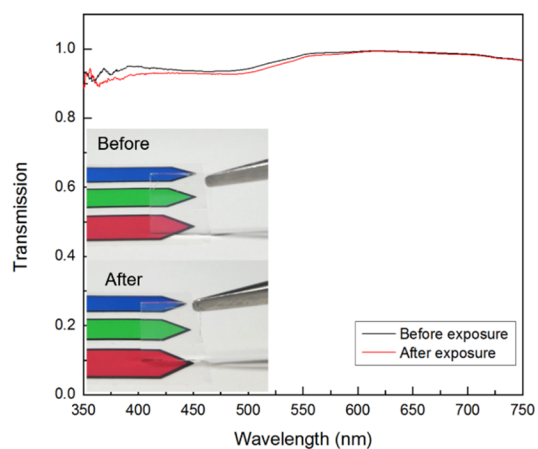


Figure A-2-8 Transmission of the pure silk film on quartz substrate before/after exposure to HCl vapor. Insets show photographs of the clearance and transparency of the silk film.

## A.4. Summary

Physically transient, large area, and cost-effective surface-emitting DFB lasers were reported using an aqueous mixture (silk bio-ink) of two biomedical materials: silk fibroin (matrix) and sodium fluorescein (dopant). I was able to obtain a silk DFB laser by spin-coating the silk bio-ink on a large area of a permanently usable 1D glass grating. The realized silk DFB laser exhibited polarized single mode lasing at 555 nm with a threshold of 13.6 mJ/cm<sup>2</sup>. These lasing wavelengths and thresholds were strongly maintained in multiple trials. The proposed scheme of the device was applied as a laser-based chemosensor for the detection of HCl vapor. A short exposure to HCl vapor deteriorated the quantum efficiency of the sodium fluorescein through the chemically stable silk matrix and consequently induced the silk DFB laser quenching of the laser output. A deteriorated silk DFB laser after use could be simply removed using water and then replaced by spin-coating the silk bio-ink again. In addition, the material traits of silk fibroin including the biocompatibility, biodegradability, and stable conservation of bio-dopants would be advantageous for bio-optical applications such as implantable bio-optical sensors and wireless stimulation of cell.

# References

- [1] R. Freeman, J. Boekhoven, M. B. Dickerson, R. R. Naik, S. I. Stupp, “Biopolymers and supramolecular polymers as biomaterials for biomedical applications,” *MRS Bulletin* **40**, 1089-1101 (2015).
- [2] S. Nizamoglu, M. C. Gather, M. Humar, M. Choi, S. Kim, K. S. Kim, S. W. Hahn, G. Scarcelli, M. Randolph, R. W. Redmond, S. H. Yun, “Bioabsorbable polymer optical waveguides for deep-tissue photomedicine,” *Nature Communications* **7**, 10374 (2016).
- [3] F. G. Omenetto, D. L. Kaplan, “A new route for silk,” *Nature Photonics* **2**, 641-643 (2008).
- [4] E. M. Pritchard, P. B. Dennis, F. G. Omenetto, R. R. Naik, D. L. Kaplan, “Physical and chemical aspects of stabilization of compounds in silk,” *Biopolymers* **97**, 479-498 (2012).
- [5] S. Kim, B. Marelli, M. A. Brenckle, A. N. Mitropoulos, E.-S. Gil, K. Tsioris, H. Tao, D. L. Kaplan, F. G. Omenetto, “All-water-based electron-beam lithography using silk as a resist,” *Nature Nanotechnology* **9**, 306-310 (2014).
- [6] J. Park, S.-G. Lee, B. Marelli, M. Lee, T. Kim, H.-K. Oh, H. Jeon, F. G. Omenetto, S. Kim, “Eco-friendly photolithography using water-developable pure silk fibroin,” *RSC Advances* **6**, 39330-39334 (2016).
- [7] H. Tao, B. Marelli, M. Yang, B. An, M. S. Onses, J. A. Rogers, D. L. Kaplan, F. G. Omenetto, “Inkjet printing of regenerated silk fibroin: From printable forms to printable functions,” *Advanced Materials* **27**, 4273-4279 (2015).
- [8] B. Lee, H. Kwon, S. Kim, F. Rotermund, “Natural silk protein as a new broadband nonlinear optical material,” *Optical Materials Express* **6**, 993-1002 (2016).

- [9] S. Kim, A. N. Mitropoulos, J. D. Spitzberg, H. Tao, D. L. Kaplan, F. G. Omenetto, "Silk inverse opals," *Nature Photonics* **6**, 818-823 (2012).
- [10] Y. Y. Diao, X. Y. Liu, G. W. Toh, L. Shi, J. Zi, "Multiple structural coloring of silk-fibroin photonic crystals and humidity-responsive color sensing," *Advanced Functional Materials* **23**, 5373-5380.
- [11] S. Kim, A. N. Mitropoulos, J. D. Spitzberg, D. L. Kaplan, F. G. Omenetto, "Silk protein based hybrid photonic-plasmonic crystal," *Optics Express* **21**, 8897-8903 (2013).
- [12] Y. Choi, H. Jeon, S. Kim, "A fully biocompatible single-mode distributed feedback laser," *Lab on a Chip* **15**, 642-645 (2015).
- [13] S. Toffanin, S. Kim, S. Cavallini, M. Natali, V. Benfenati, J. J. Amsden, D. L. Kaplan, R. Zamboni, M. Muccini, F. G. Omenetto, "Low-threshold blue lasing from silk fibroin thin films," *Applied Physics Letters* **101**, 091110 (2012).
- [14] R. R. D' Silva, C. T. Dominguez, M. V. D' Santos, R. B. Silva, M. Cavicchioli, L. M. Christovan, L. S. A. D' Melo, A. S. L. Gomes, C. B. D' Araujo, S. J. L. Ribeiro, "Silk fibroin biopolymer films as efficient hosts for DFB laser operation," *Journal of Materials Chemistry C* **1**, 7181-7190 (2013).
- [15] M. Lee, H. Jeon, S. Kim, "A highly tunable and fully biocompatible silk nanoplasmonic optical sensor," *Nano Letters* **15**, 3358-3363 (2015).
- [16] H. Kwon, S. Kim, "Chemically tunable, biocompatible, and cost-effective metal-insulator-metal resonators using silk protein and ultrathin silver films," *ACS Photonics* **2**, 1675-1680 (2015).
- [17] H. Tao, J. J. Amsden, A. C. Strikwerda, K. Fan, D. L. Kaplan, X. Zhang, R. D. Averitt, F. G. Omenetto, "Metamaterial silk composites at terahertz frequencies," *Advanced Materials* **22**, 3527-3531 (2010).

- [18] H. Tao, A. C. Strikwerda, M. Liu, J. P. Mondia, E. Ekmekci, K. Fan, D. L. Kaplan, W. J. Padilla, X. Zhang, R. D. Averitt, F. G. Omenetto, "Performance enhancement of terahertz metamaterials on ultrathin substrates for sensing applications," *Applied Physics Letters* **97**, 261909 (2010).
- [19] A. Camposeo, P. D. Carro, L. Persano, K. Cyprych, A. Szukalski, L. Sznitko, J. Mysliwiec, D. Pisignano, "Physically transient photonics: Random versus distributed feedback lasing based on nanoimprinted DNA," *ACS Nano* **8**, 10893-10898 (2014).
- [20] M. Brenckle, H. Cheng, S. Hwang, H. Tao, M. Paquette, D. L. Kaplan, J. A. Rogers, Y. Huang, F. G. Omenetto, "Modulated degradation of transient electronic devices through multilayer silk fibroin pockets," *ACS Applied Materials & Interfaces* **7**, 19870-19875 (2015).
- [21] C. Dagdeviren, S.-W. Hwang, Y. Su, S. Kim, H. Cheng, O. Gur, R. Haney, F. G. Omenetto, Y. Huang, J. A. Rogers, "Transient, biocompatible electronics and energy harvesters based on ZnO," *Small* **9**, 3398-3404 (2013).
- [22] J. Clark, G. Lanzani, "Organic photonics for communications," *Nature Photonics* **4**, 438 (2010).
- [23] A. Rose, Z. Zhu, C. F. Madigan, T. M. Swager, V. Bulović, "Sensitivity gains in chemosensing by lasing action in organic polymers," *Nature* **434**, 876 (2005).
- [24] Y. Wang, P. O. Morawska, A. L. Kanibolotsky, P. J. Skabara, G. A. Trunbull, I. D. Samuel, "LED pumped polymer laser sensor for explosives," *Laser & Photonics Reviews* **7**, L71-L76 (2013).
- [25] M. Ramuz, D. Leuenberger, R. Pfeiffer, L. Bürgi, C. Winnewisser, "OLED and OPD-based mini-spectrometer integrated on a single-mode planar waveguide chip," *European Physical Journal Applied Physics* **46**, 12510 (2009).

- [26] T. Rabe, K. Gerlach, T. Riedl, H. –H. Johannes, W. Kowalsky, J. Niederhofer, W. Gries, J. Wang, T. Weimann, P. Hinze, F. Galbrecht, U. Scherf, “Quasi-continuous-wave operation of an organic thin-film distributed feedback laser,” *Applied Physics Letters* **89**, 081115 (2006).
- [27] J. K. Singh, F. E. Dhawahir, A. F. A. Hamid, P. B. Chell, “The use of dye in ophthalmology,” *Journal of Audiovisual Media in Medicine* **27**, 62-67 (2004).
- [28] S. Kim, S. Ahn, J. Lee, H. Jeon, P. Regreny, C. Seassal, E. Augendre, L. D. Cioccio, “Milliwatt-level fiber-coupled laser power from photonic crystal band-edge laser,” *Optics Express* **19**, 2105-2110 (2011).
- [29] H. Kim, H. Jung, D.-H. Lee, K. B. Lee, H. Jeon, “Period-chirped gratings fabricated by laser interference lithography with a concave Lloyd's mirror,” *Applied Optics* **55**, 354-359 (2016).
- [30] C. Ye, L. Shi, J. Wang, D. Lo, X.-I. Zhu, “Simultaneous generation of multiple pairs of transverse electric and transverse magnetic output modes from titania zirconia organically modified silicate distributed feedback waveguide lasers,” *Applied Physics Letters* **83**, 4101-4103 (2003).
- [31] M. Lu, S. S. Choi, U. Irfan, B. T. Cunningham, “Plastic distributed feedback laser biosensor,” *Applied Physics Letters* **93**, 111113 (2008).
- [32] L. Persano, A. Camposeo, P. D. Carro, V. Fasano, M. Moffa, R. Manco, S. D'Agostino, D. Pisignano, “Distributed feedback imprinted electrospun fiber lasers,” *Advanced Materials* **26**, 6542-6547 (2014).
- [33] M. M. Martin, L. Lindqvist, “The pH dependence of fluorescein fluorescence,” *Journal of Luminescence* **10**, 381-390 (1975).

- [34] G. Tsiminis, Y. Wang, A. L. Kanibolotsky, A. R. Inigo, P. J. Skabara, I. D. W. Samuel, G. A. Turnbull, "Nanoimprinted organic semiconductor laser pumped by a light-emitting diode," *Advanced Materials* **25**, 2826-2830 (2013).
- [35] R. Sjöback, J. Nygren, M. Kubista, "Absorption and fluorescence properties of fluorescein," *Spectrochimica Acta Part A: Molecular and Biomolecular Spectroscopy* **51**, L7-L21 (1995).



## Chapter 4

### Conclusion and perspective

In this thesis, I proposed and demonstrated hybrid type PhC lasers composed of CQDs and passive backbone structures and their applications.

First, efficient platform for on-chip integration of CQD PhC laser and passive components is suggested. Silicon nitride is interesting material, which can be treated by CMOS-compatible process and also has relatively high refractive index and broad optical transparency from visible to near-infrared wavelength range. With combination of silicon nitride and CQDs gain materials, hybrid PhC lasers and passive devices are efficiently integrated in a way where silicon nitride waveguiding layer is shared by various components. A conceptual PIC is experimentally demonstrated, in which a PhC band-edge laser, a slab waveguide, and output couplers are all integrated on a single chip. Under excitation condition, coherent single-mode laser is emitted with well-defined in-plane emission directions, and subsequently coupled into the passive waveguide layer with a guaranteed high coupling efficiency. This configuration for active and passive photonic devices on a chip could be an alternative picture of conventional silicon-based PIC in near future.

In the second research topic, continuously tunable DFB laser device composed of CQD film on chirped grating is introduced. To make hybrid type tunable laser source composed of CQD and fused silica, high-throughput LIL method is employed instead of writing the entire nano-patterns by conventional electron beam lithography. To make efficiently line gratings chirped, Lloyd's LIL configuration is modified by introducing cylindrical mirror parts. Also, CQD film is transferred onto wet-transfer

method, which are intended for flat and dense CQD film to be positioned on the arbitrary substrate. Single-mode, surface-emitting DFB laser structures are numerically designed by FDTD method. Also, laser wavelengths are observed to be progressively varied as optical excitation positions are translated in photoluminescence experiments. Continuously tunable coherent light source could be useful itself in a variety of applications. Moreover, the results demonstrate modified LIL method can produce high quality chirped gratings at less effort, which could be helpful for other sophisticated photonic devices.

In the appendant topic, bio-compatible silk DFB laser with physically transient characteristics are demonstrated. It is a kind of bio-compatible version of hybrid PhC laser composed of silk, fused silica, dyes. Silk fibroin is natural protein extracted from *Bombyx mori* caterpillar and draw public attention for its self-assembling property at optical wavelengths scale and optical transparency. The silk bio-ink, bio-compatible silk materials combined with sodium fluorescein dye commonly used for diagnostics in ophthalmology and optometry, is spin-casted on the robust fused silica grating substrate for DFB lasing. The organic device has limited lifetime due to the degradability of dye but silk active layer can be easily removed by dipping in water, and by re-coating the bio-ink new device can be obtained without difficulties. In addition, chemosensing capability for detecting hydrochloride vapor is also investigated.

In conclusion, in this these, I suggested hybrid type PhC laser of passive structural backbone and external gain material, especially CQDs. Efficient on-chip integrated coherent laser sources with passive structures are demonstrated, and tunable laser sources from efficient fabrication method are presented. These results are expected to contribute to the understanding of various optical devices and PIC, as

well as to the efficient implementation.

## Abstract in Korean

광자 결정은 유전상수가 다른 2가지 혹은 그 이상의 물질이 전자기파의 파장 스케일에 주기적으로 배열된 구조를 말한다. 이 구조는 이온 격자가 주기적인 포텐셜에서 전자의 운동에 영향을 주는 것과 유사한 방식으로, 광자의 운동에 영향을 미친다. 광자 결정을 통과하는 전자기파는 균일한 매질을 통과 할 때 볼 수 없는 특별한 광 분산 관계를 가지고 있다. 광자 결정 내의 광 분산 관계에서 대표적으로 나타나는 광학적 특성으로는 광 밴드갭과 이상군속도 현상이 있는데, 광 밴드 갭은 광자의 상태가 존재할 수 없는 특정 주파수 영역이며, 이상군속도 현상의 하나인 광 밴드 엣지 상태에서는 광 모드의 군속도는 0에 근접한다. 두 가지 광학적 개념은, 각각 강하게 국지화된 공동 구조 또는 공간적으로 확장된 정상파 공진 형태에서 전자기파를 가두는데 사용될 수 있으며, 이 경우 광 이득 물질과 광자 간의 상호작용이 현저하게 증가 될 수 있다.

광자 결정은 작은 공간영역에서 제작 될 수 있고, 이를 이용해 간섭성 광원을 생성 할 때 전력 소비가 적으며 모드 특성을 설계할 수 있다는 점에서 큰 잠재력이 있다. 이러한 광자 결정은 광 집적 회로를 위한 효율적인 광원에 활용 될 수 있다. 하이브리드 광자 결정 레이저는 빛을 내지 않는 수동형의 광학 구조와 외부의 능동형의 광 이득 물질로 구성되는데, 발광 파장 및 도파 특성 등을 선택할 때 유연성을 가지므로 고밀도 광집적회로를 구현하기 위한 뛰어난 간섭성 광원이 될 수 있다.

특히, 콜로이드 양자점은 미래의 광집적회로 구상에서 유망한 이득 물질 중 하나인데, 화학적으로 저렴하게 합성되며, 용액 공정의 이점을 가지면서 효율적으로 빛을 내는 나노 빌딩 블록의 역할을 할 수 있다. 또한, 개별 콜로이드 양자점의 크기를 조절함으로써, 양자 효율의 감소 없이 좁은 선폭의 방출 파장을 쉽게 제어할 수 있다.

이 논문에서는 첫 번째 연구 주제로, 콜로이드 양자점 광자 결정 레이저와 수동형의 소자를 하나의 칩 위에 구현하기 위한 효율적인 플랫폼을 제안하였다. 실리콘 질화물은 CMOS 공정에 호환성이 있으면서, 가시 광선에서 근적외선 파장 범위에 이르기까지 상대적으로 높은 굴절률과 넓은 광학 투명도를 가지고 있는 흥미로운 물질이다. 하이브리드 형의 광자 결정 레이저와 다양한 수동 소자는 실리콘 질화물 기반의 도파층을 공유하는 방식을 통해, 소자들 사이에 효율적인 광학적 결합 효율을 가진다. 광자 결정 밴드갭 레이저, 평면형의 도파로, 출력을 위한 커플러가 모두 하나의 칩에 통합된 개념적인 광 집적회로가 실험적으로 시연되었다. 광 여기 조건하에서, 간섭성의 단일 모드 레이저가 평면 내의 방향으로 방출되고, 이어서 높은 결합 효율을 보장하는 수동형의 도파로 층과 이어진다. 이러한 방식으로, 하나의 칩 상에 통합된 능동형 및 수동형 광학 소자 구성은 가까운 장래에 기존의 실리콘 기반의 광 집적회로의 대안이 될 수 있다.

두 번째 연구 주제에서는, 구매 있는 회절격자와 콜로이드 양자점 박막으로 이루어진 연속 파장가변 분산 피드백 레이저 소자를 소개한다. 콜로이드 양자점과 용융 실리카로 구성된 하이브리드 형의 파장가변

레이저 소스를 만들기 위해, 대면적의 나노 패턴을 기존의 전자빔 리소그래피 방법으로 제작하지 않고, 고효율의 레이저 간섭 리소그래피 방법을 사용하였다. 선형의 회절 격자 패턴을 효율적으로 제작하기 위해, 로이드 형의 간섭 리소그래피 방법의 구성을 원통형 미러를 이용해 수정하였다. 또한, 습식 전사 방법을 이용하여, 넓은 영역에 걸쳐 평평한 고밀도의 콜로이드 양자점 박막을 임의의 원하는 기판 상에 위치하도록 하였다. 그리고 단일 모드를 가지면서, 면 수직 발광 특성을 가지고 있는 분산 피드백 레이저를 유한 차분시간 영역법을 사용하여 수치적으로 설계하고, 이에 따라 제작하였다. 제작된 소자에서 레이저 파장은 광여기 위치가 점진적으로 이동함에 따라 점진적으로 변하는 것으로 관찰된다. 연속적인 파장 조절이 가능한 간섭성 광원은 다양한 응용 분야에서 유용하게 사용될 수 있다. 나아가, 수정된 레이저 간섭 리소그래피 방법은 적은 노력으로 고품질의 구배 회절 격자를 생성할 수 있음을 보여주는데, 이는 다른 정교한 광학 소자 제작에도 활용될 수 있을 것이다.

부록으로 포함된 주제에서는, 물리적으로 일시적인 특성을 지닌 생체 적합형 실크 분산 피드백 레이저를 소개한다. 이 소자는 실크, 용융 실리카, 염료로 구성된 하이브리드 광자 결정 레이저의 생체 적합형 버전이다. 실크 피브로인은 누에나방 애벌레에서 추출한 천연 단백질로, 광학 투명도를 가지고 광학 파장 스케일에서 자가 조립 특성을 가지고 있어 대중의 관심을 끌고 있다. 실크 바이오 잉크는 생체 적합성 실크 물질과 안과 및 검안 과정에서 일반적으로 사용되는 플루오레세인나트륨

염료를 결합한 것인데, 견고한 용융 실리카 회절 격자 기판 위에 이를 스핀 캐스팅하는 방법으로 분산 피드백 레이저 소자를 제작하였다. 이 유기 소자의 경우, 염료의 분해성으로 인해 수명이 제한적이다. 하지만, 실크 바이오 잉크로 형성되는 활성층은 물에 담그어 녹여내는 방식으로 쉽게 제거할 수 있으며, 다시 스핀캐스팅 하는 방식으로 새 소자를 어렵지 않게 제작할 수 있다. 또한 이 소자를 통해 염산 증기를 화학적으로 검출하기 위한 가능성도 확인하였다.

결론적으로, 이 논문에서 수동형의 뼈대 구조와 외부의 광 이득 물질로 이루어진 하이브리드 형의 광자 결정 레이저를 제안하였다. 특히, 주로 콜로이드 양자점을 광 이득 물질로 사용하였는데, 수동형의 소자와 간섭성의 레이저 광원을 효율적으로 하나의 칩에 결합한 플랫폼을 소개하였고, 또한, 효율적인 방법으로 제작한 파장가변 레이저 광원을 소개하였다. 이 연구 결과들은 다양한 광 소자 및 광 집적회로에 대한 이해, 나아가 효율적인 구현에 기여할 것으로 기대한다.

**주요어:** 광자 결정, 하이브리드 광자결정 레이저, 콜로이드 양자점, 온-칩 결합, 파장가변 레이저

**학번:** 2011-20424